AGU PUBLICATIONS

JGR

Journal of Geophysical Research: Atmospheres

RESEARCH ARTICLE

10.1002/2016JD025674

Key Points:

- AIRS data are used to estimate the vapor flux over the Greenland ice sheet
- Vapor flux is improved with ice specific parameterizations
- Vapor fluxes were similar when compared with RACMO2.3

Correspondence to:
L. N. Boisvert,
linette.n.boisvert@nasa.gov

Citation:
Boisvert, L. N., J. N. Lee, J. T. M. Lenaerts, B. Noël, M. R. van den Broeke, and A. W. Nolin (2017), Using remotely sensed data from AIRS to estimate the vapor flux on the Greenland ice sheet: Comparisons with observations and a regional climate model, *J. Geophys. Res. Atmos.*, *122*, 202–229, doi:10.1002/2016JD025674.

Received 19 JUL 2016
Accepted 19 DEC 2016
Accepted article online 22 DEC 2016
Published online 11 JAN 2017

Using remotely sensed data from AIRS to estimate the vapor flux on the Greenland ice sheet: Comparisons with observations and a regional climate model

Linette N. Boisvert[1], Jae N. Lee[2], Jan T. M. Lenaerts[3], Brice Noël[3], Michiel R. van den Broeke[3], and Anne W. Nolin[4]

[1]Earth System Science Interdisciplinary Center (ESSIC), University of Maryland, College Park, Maryland, USA, [2]Joint Center for E and Technology (JCET), University of Maryland, Baltimore County, Baltimore, Maryland, USA, [3]Institute for Marine and Atmospheric Research, Utrecht University, Utrecht, Netherlands, [4]College of Earth, Ocean, and Atmospheric Sciences, Oregon State University, Corvallis, Oregon, USA

Abstract Mass loss from the Greenland ice sheet (GrIS) in recent years has been dominated by runoff from surface melt. It is currently being studied extensively, while little interest has been given to the smallest component of surface mass balance (SMB): the vapor flux. Although poorly understood, it is not negligible and could potentially play a larger role in SMB in a warming climate where temperature, relative humidity, and precipitation changes remain uncertain. Here we present an innovative approach to estimate the vapor flux using the Atmospheric Infrared Sounder (AIRS) version 6 data and a modified vapor flux model (BMF13) over the GrIS between 2003 and 2014. One modification to the BMF13 model includes a new Multiangle Imaging SpectroRadiometer surface aerodynamic roughness product, which likely produces more accurate estimates of the drag coefficient on the ice sheet. When comparing AIRS data with GC-Net and Programme for Monitoring of the Greenland Ice Sheet automatic weather station observations of skin temperature, near-surface air temperature, and humidity, they agree within 2 K, 2.68 K, and 0.34 g kg^{-1}. Largest differences occur in the ablation zone where there is significant subgrid heterogeneity. Overall, the average vapor flux from the GrIS between 2003 and 2014 was found to be 14.6 ± 3.6 Gt yr^{-1}. No statistically significant trends were found during the data record. This data set is compared to the Regional Atmospheric Climate Model (RACMO2.3) vapor flux, and BMF13 produced smaller vapor fluxes in the summer (~0.05 Gt d^{-1}) and slightly more deposition in the winter (~9.4×10^{-3} Gt d^{-1}). Annually, differences between BMF13 and RACMO2.3 were only 30 ± 15%.

1. Introduction

In recent years, mass loss from the Greenland ice sheet (GrIS) has accelerated [*Chen et al.*, 2006; *Zwally et al.*, 2011; *Kahn et al.*, 2014; *Velicogna et al.*, 2014]. GrIS mass loss between 1990 and 2008 is attributed equally to increased solid ice discharge through its outlet glaciers and enhanced runoff from surface melt [*Van den Broeke et al.*, 2009; *Shepherd et al.*, 2012], while surface meltwater runoff has dominated post 2008 mass losses [*Enderlin et al.*, 2014]. Surface melt is enhanced by a darkening of the ice sheet [*Hall et al.*, 2013] due to a decrease in surface albedo [*He et al.*, 2013], resulting in a lengthening of the melt season [*Mote*, 2007; *Tedesco et al.*, 2011] as well as increasing the melt area [*Mernild et al.*, 2011; *Fettweis et al.*, 2013].

This marked mass loss, especially around the ice sheet margins [*Wang et al.*, 2014], is offset by the slight interior thickening of the GrIS, which has been attributed to a small increase in snowfall [*Johannessen et al.*, 2005; *Seo et al.*, 2015]. Future sustained GrIS mass loss, and associated sea level rise, is expected to be dominated by surface runoff [*Vizcaino et al.*, 2014], which is not expected to be compensated by an increase in precipitation [*Van Angelen et al.*, 2012]. Precipitation and surface runoff are the dominant source and sink terms of the GrIS surface mass balance (SMB), respectively. Multiple studies have looked into surface melting and runoff amounts from the ice sheet and peripheral glaciers [*Howat et al.*, 2007; *Hanna et al.*, 2008; *Sundal et al.*, 2011; *Enderlin et al.*, 2014] and also at changes and amount of precipitation that occur on the ice sheet [*Schuenemann and Cassano*, 2010; *Mernild et al.*, 2015].

Relatively little attention has been given to the smallest component of GrIS SMB, i.e., the vapor flux which consists of sublimation/deposition and evaporation. The reason for this is that the water vapor concentration

in cold environments is often poorly known, because few in situ observations are made in the harsh environment, and moreover, the vapor flux cannot be measured directly at unmanned stations [*Box and Steffen*, 2001]. Little attention is given to the term, because it is assumed to be relatively small in comparison to precipitation and runoff, although it is certainly not negligible. The future contribution of the vapor flux to the overall SMB of the GrIS depends on how the lower atmosphere over the GrIS will respond to climate change, which currently remains uncertain [*Woldemeskel et al*., 2012]. If air temperatures and humidity increase, more deposition could occur in the winter months, and less sublimation and evaporation (i.e., mass loss) could occur in the summer months, leading to a net decrease in GrIS mass loss through the vapor flux. If air temperatures increase, but humidity decreases or does not change, an opposite effect can be expected, when a higher vapor flux is likely to occur in the summer months, but less deposition will occur in the winter. As more melt ponds form on the ice sheet [*Echelmeyer et al*., 1991; *Sneed and Hamilton*, 2007], evaporation can be enhanced, increasing mass loss. Regardless of how the vapor flux of the ice sheet will change in the future, it remains an essential part of the SMB and accurate estimates are needed to assess the mass balance of the ice sheet.

Using an extrapolation of GC-Net automatic weather station data, *Box and Steffen* [2001] estimated the vapor flux over Greenland between 1999 and 2000 at 120 Gt yr^{-1}, suggesting that this single component removes roughly 23% of the annual precipitation. Regional climate models and atmospheric reanalysis have also been used to study the vapor flux over the GrIS [*Ohmura et al*., 1999; *Ettema et al*., 2010b; *Lenaerts et al*., 2012]. Due to the sparsely available in situ observational data, it remains challenging to evaluate the performance of these models in simulating GrIS vapor flux.

In recent years, satellite data have shown considerable improvements in estimating near-surface air temperature and humidity using new retrieval techniques [*Dong et al*., 2010]. For example, using a hyperspectral technique, the Atmospheric InfraRed Sounder (AIRS) on board NASA's Aqua satellite is able to measure temperature and humidity under almost all meteorological conditions [*Susskind et al*., 2003], and this data set is of great value for estimation of surface moisture fluxes on a global scale.

In this paper we introduce a new, independent vapor flux data set comprising the full GrIS for the period 2003–2014 that is created using remotely sensed data from AIRS and a model adapted from *Boisvert et al*. [2013] that was created for use over Arctic sea ice. This data product is compared with in situ observations and also an independent regional atmospheric climate model.

2. Data and Model

2.1. Atmospheric Infrared Sounder Data Products

The Atmospheric Infrared Sounder (AIRS) is a cross-track high spectral resolution infrared sounder on board NASA's Aqua satellite that was launched on 4 May 2002. AIRS collects radiance data with a 13.5 km spatial resolution in the horizontal at nadir and has 2378 infrared channels from which highly accurate and quality-controlled geophysical products are generated dealing with the Earth and its atmosphere [*Susskind et al*., 2011, 2014]. AIRS has twice daily, global coverage in ascending and descending orbits and allows for accurate retrievals under most cloud conditions, which is important in the Polar Regions, where data are sparse and clouds are prevalent. AIRS Level 3 data products are generated on a 1° by 1° latitude-longitude grid by including all Level 2 retrieved values in that grid box which have quality control flags representing retrievals thought to be of highest and of good quality. Average daily products are produced using data from both ascending and descending orbits.

Retrieval steps are done sequentially, and surface skin temperature, near-surface air temperature, and surface and near-surface specific humidity are all derived independently of each other [*Susskind et al*., 2014]. Globally, roughly 80% of all retrievals at the surface are flagged as best or good quality in version 6. The use of NeuralNet, a high-quality training data set derived from models and operational data measurements, is used to train algorithms for retrievals of geophysical parameters [*Blackwell*, 2012]. This first guess improves retrievals of near-surface temperature and water vapor and also allows for high-quality retrievals under almost all cloud conditions. The AIRS retrieval process is unique in that it is able to measure surface properties under almost all sky conditions without the need of surface type classification [*Susskind et al*., 2003], whereas most satellite retrievals of surface products treat land, ocean, and sea ice surfaces differently and require classification of a

scene for surface type and clear cloudy sky prior to the retrieval. This creates additional retrieval errors and also a bias toward clear-sky conditions.

The AIRS algorithm employs the cloud-clearing radiance approach iteratively within its retrieval algorithm, such that the retrievals produce the best fit to the final cloud-clear radiances. Using the nine 15 km hyperspectral IR measurements inside a 50 km multichannel microwave footprint, this technique is able to take advantage of cloud inhomogeneity in a smooth clear-sky background to estimate what cloud-clear radiances should be as cloud fraction approaches zero, even where all nine IR footprints are cloudy [*Susskind et al*., 2014].

Due to the high elevation of Greenland, the 1000 hPa temperature and relative humidity AIRS data products could not be used to compute the specific humidity of the air which was previously done for the Arctic [*Boisvert et al*., 2013, 2015a]. Thus, a blended air temperature and relative humidity daily product was created using data from 1000, 925, 850, 700, and 600 hPa, if data from these levels were available. Greenland's elevation was taken from a Digital Elevation Model created based on data from the Geoscience Laser Altimeter System on board the Ice, Cloud and land Elevation Satellite [*DiMarzio et al*., 2007]. This elevation was then subtracted from the blended geopotential height product to determine the height above the surface at which each temperature and humidity value was taken.

2.2. ERA-Interim Wind Speed Product

Daily averaged wind speeds at 10 m are taken from the European Center for Medium-Range Weather Forecast (ECMWF) ERA-Interim full resolution (http://www.ecmwf.int/en/research/climate-reanalysis/era-interim). ERA-Interim data are available at a 0.72° spatial resolution. It combines a model-based first-guess field along with in situ and remotely sensed data into an assimilated data set using the 4D-VAR method [*Dee et al*., 2011].

2.3. Surface Roughness Product

On the GrIS, surface roughness is created by glacier dynamics and surface-atmosphere interactions. The surface roughness is important, because it affects boundary layer processes through the aerodynamic roughness length. A surface roughness data product from the Multiangle Imaging SpectroRadiometer (MISR) [*Nolin et al*., 2002] is used in this study to improve on the use of surface roughness parameters that are assumed constant in space and time. This data set, which is only valid between March and July, i.e., during the sunlit season, consists of average roughness lengths from 2000 to 2013 and is created via MISR angles of ±60° and nadir that have been calibrated against roughness data from the Airborne Topographic Mapper (ATM). The ATM and MISR data were combined to create a 4-D model where MISR images could be converted to surface roughness. *Nolin et al*. [2002] compared the MISR roughness product with ATM transects over Jakobshavn Glacier and found an average correlation of $R^2 = 0.71$. An example of this surface roughness product is shown for July 2012 in Figure 1d. There are some data gaps in the roughness product where no reliable estimates could be made. These gaps will show up in a single month but will be averaged out when looking at the 2003–2014 time series.

2.4. BMF13 Model

To calculate the vapor flux over Greenland, the skin temperature, blended air temperature, blended relative humidity, and blended geopotential height products from AIRS are used along with the ERA-Interim 10 m wind speed and the MISR surface roughness. These data are put into the *Boisvert et al*. [2013] moisture flux model (herein BMF13) with a few adaptations made for Greenland. Vapor flux is estimated from equation (1):

$$E = \rho C_{Ez} S_r \left(q_{s,i} - q_z\right) \tag{1}$$

where ρ is the air density (kg m^{-3}), C_{Ez} the water vapor transfer coefficient (unitless), S_r the effective wind speed (m s^{-1}), $q_{s,i}$ is the saturation specific humidity over the ice/snow surface (kg kg^{-1}), and q_z is the air specific humidity at 2 m (kg kg^{-1}). The vapor flux is estimated from (1) using Monin-Obukhov similarity theory and an iterative calculation scheme based on *Launiainen and Vihma* [1990] with a few modifications: we use the flux algorithm of *Grachev et al*. [2007] for stable conditions over ice and the effective wind speed, which includes a parameter for gustiness that is different in stable and unstable boundary conditions [*Andreas et al*., 2010]. By using the effective wind speed we prevent the transfer coefficients from approaching infinity when the wind speed approaches zero. The MISR roughness values are used to calculate C_{Ez} in (1) and average roughness values range from 11 cm in April to roughly 20 cm in July. For the remainder of the

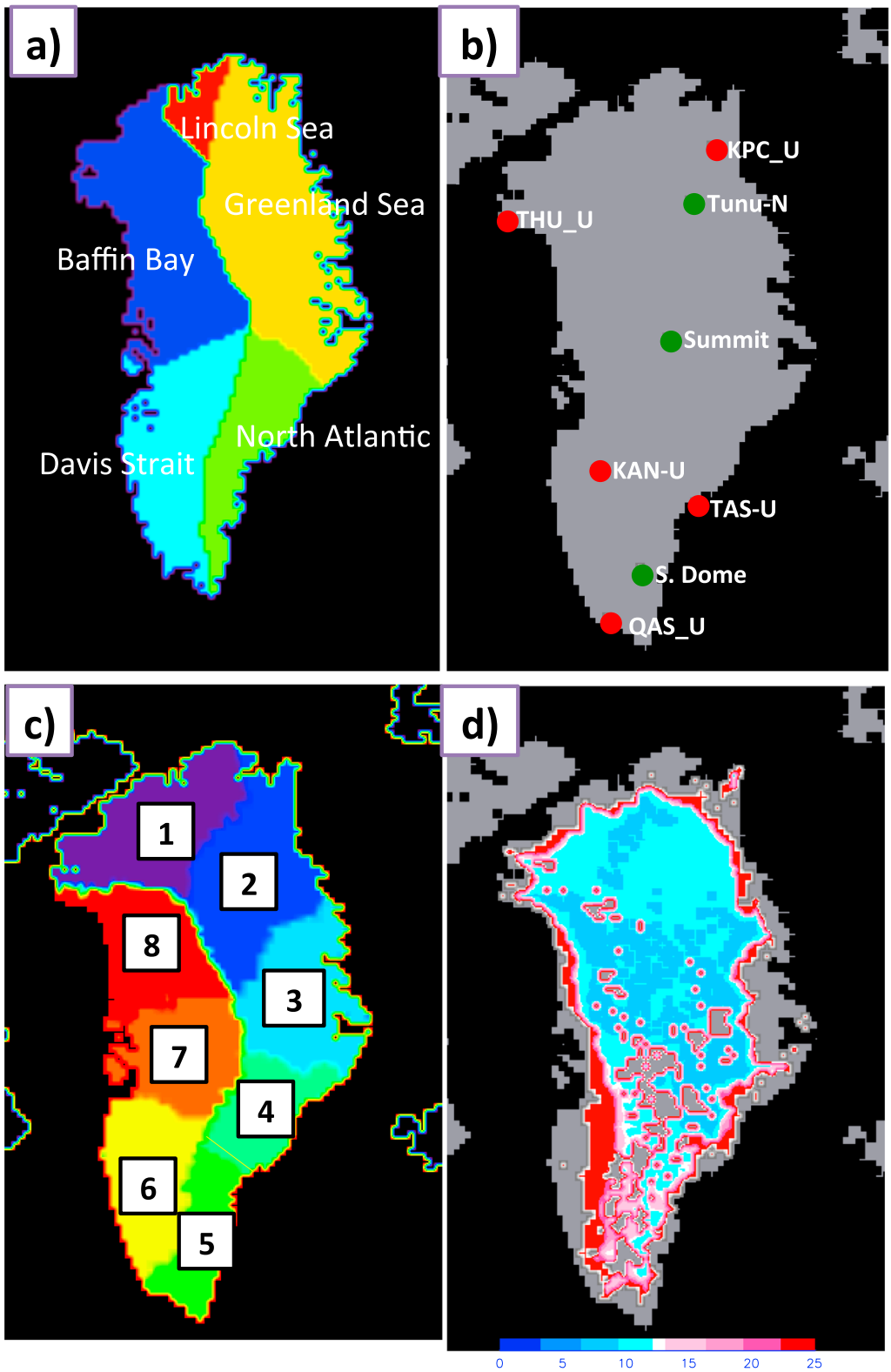

Figure 1. (a) Map of Greenland split into different atmospheric regimes (dark blue: Baffin Bay, light blue: Davis Strait, green: North Atlantic, yellow: Greenland Sea, and red: Lincoln Sea). (b) Automatic Weather Stations (AWS) in the Greenland Climate Network (GC-Net) denoted by the green circles and PROMICE data denoted by the red circles. (c) Map of Greenland split into eight different drainage basins (source: *Wouters et al.* [2008]). (d) Surface roughness product produced from MISR for July 2012.

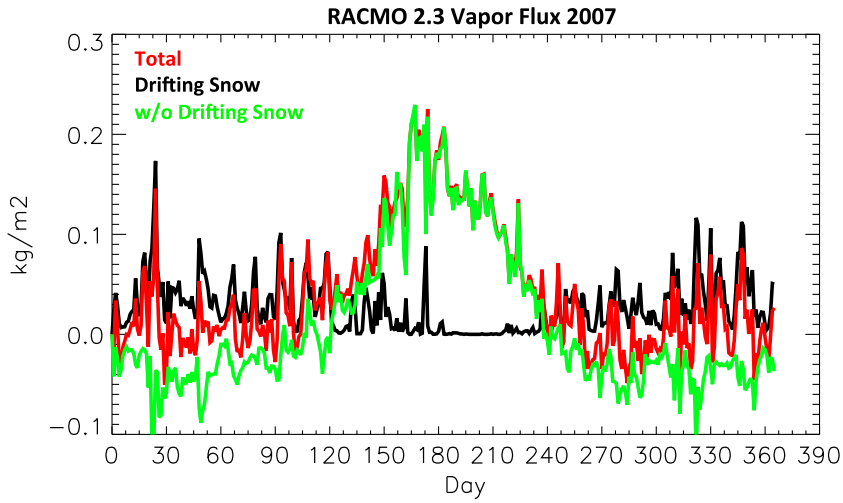

Figure 2. RACMO2.3 vapor flux for the GrIS in 2007. Black is the drifting snow sublimation, green is the vapor flux only where the drifting snow sublimation is zero (used for comparison with BMF13), and red is the total vapor flux.

year, when data were not available, an average value of 10 cm was used because the surface roughness has shown to increase throughout the year, with maxima seen in the summer months [*Smeets and van den Broeke*, 2008], where in the winter the surface is not as rough due to snow covering the bare ice.

The iterative method allows for the use of input variables (i.e., air temperature, relative humidity, and wind speed) to be measured at varying heights above the surface. This method uses input variables at different heights (geopotential height minus surface elevation) and along with the stability of the boundary layer, estimates their value at a reference height of 2 m. E is calculated each day between 2003 and 2014 for each 25 km^2 pixel in the polar stereographic grid over the Greenland ice sheet. Sublimation is positive when directed from the surface to the atmosphere (surface mass loss); deposition is negative and defined as going from the atmosphere to the surface (surface mass gain).

2.5. RACMO2.3

Vapor flux output from the Regional Atmospheric Climate Model version 2.3 (RACMO2.3) focused on the GrIS [*Noel et al.*, 2015] is used to compare with the BMF13 product. RACMO2.3 is forced by ERA-Interim at its lateral boundaries and combines two weather prediction models: dynamics from the High Resolution Limited Area Model [*Unden et al.*, 2002] and physical processes from ECMWF [*ECMWF-IFS*, 2008]. There have been many improvements made to RACMO2.3 to produce a more realistic simulation of the polar climate, including drifting snow processes [*Lenaerts et al.*, 2012], a physical snow albedo scheme adapted for Greenland conditions [*Kuipers Munneke et al.*, 2011; *Van Angelen et al.*, 2012], and updated cloud physics [*Van Wessem et al.*, 2014]. RACMO2.3 data are provided daily with an 11 km spatial resolution.

Ettema et al. [2010a] evaluated RACMO2.1 2 m air temperature and specific humidity between 2003 and 2007 using a number of in situ observations from automated weather station (AWS). Over the entire ice sheet they found a positive bias of 0.9°C and an RMSE of 2.3°C in 2 m air temperature, and a negative bias of −0.05 g/kg and an RMSE of 0.29 g kg^{-1} in 2 m specific humidity. Largest biases were found along the southeast coast, and while biases are small in the ablation zone, they increase toward the ice sheet margin. This is very similar to the results found when comparing AIRS with the GC-Net and Programme for Monitoring of the Greenland Ice Sheet (PROMICE) station data, with AIRS producing an RMSE of 2.68°C for 2 m air temperature 0.34 g kg^{-1} for 2 m specific humidity, discussed earlier. More specifically, *Ettema et al.* [2010a] found that in the winter months, RACMO2.1 tended to underestimate the air temperature and the relative humidity more than in the summer. A detailed evaluation of RACMO2.1 simulated vapor flux has so far been hampered by the limited availability of observational data.

It is important to note that the RACMO2.3 vapor flux product that we use here includes drifting snow sublimation [*Lenaerts et al.*, 2012]. Although drifting snow sublimation is an important feature on the ice sheet, AIRS data and the BMF13 model do not allow for calculation of this term. Figure 2 shows the daily GrIS vapor

flux for 2007 from RACMO2.3. From this figure, which is consistent with *Lenaerts et al*. [2012], we see that drifting snow sublimation is largest in the winter and basically nonexistent in the summer. When this term is included in the total vapor flux, it reduces the negative flux (deposition), creating a positive flux (sublimation) especially in the winter months. Thus, in order to compare accurately with the BMF13 model, we will only use data points where there is no drifting snow sublimation present in RACMO2.3.

In order to compare vapor flux output from both RACMO2.3 and BMF13, we have interpolated them onto a 25 km^2 polar stereographic grid.

3. Quality of AIRS Data and Error Estimation

We compare the AIRS products with automated weather station (AWS) data in order to determine whether the BMF13 model using AIRS data can be used to reliably estimate Greenland vapor flux. Skin temperature, air temperature, and specific humidity from AIRS are compared to in situ observations between 2003 and 2014 from three separate AWS in the north (Tunu-N), middle (Summit), and south (South Dome) of the accumulation zone of Greenland (Figure 1b) [*Steffen et al*., 1996]. These are part of the total of 18 AWS that constitute the Greenland Climate Network (GC-Net), which was started in 1995. GC-Net provides reasonable coverage of the ice sheet, and the majority of the stations are located at elevations higher than 2 km. GC-Net AWS are prone to errors in data collection in harsh environments, such as the GrIS, where low temperatures often occur and snow/ice can accrete on the instruments. Thus, *Steffen et al*. [1996] have done extensive quality control and also interpolation when data are missing. Detailed information on the GC-Net measurements can be found in *Box and Steffen* [2001]. In situ data from the Programme for Monitoring of the Greenland Ice Sheet (PROMICE) [*Ahlstrom et al*., 2008] stations along the ablation zone of Greenland are also used for validation of AIRS data (Figure 1b). These stations include: THU_U, KAN_M, QAS_U, TAS_U, and KPC_U, and monthly data air temperature and specific humidity at roughly 2.7 m above the surface from 2008 to 2014 are used. By comparing with in situ measurements, we can determine errors for each individual AIRS data product, which helps to assess the reliability of the BMF13 vapor flux product.

Figure 3 shows monthly skin temperatures from AIRS and near-surface air temperature (taken at ~1.4 m above the surface) from the GC-Net stations for 2003–2014. At all three AWS, AIRS show very good agreement with the observations, both for the annual cycle and for interannual variability. At Tunu-N and Summit, the summer skin temperatures tend to have a slight cold bias (~2.5 K) and some years have a slight cold bias in the winter months as well. At South Dome AWS, there does not appear to be a cold bias in the summer months, although a few years show a cold bias in the winter months. The skin temperatures from AIRS are compared with the lowest air temperatures (1.4 m) from the AWS, thus it would be expected that the skin temperature from AIRS would be lower and explains the cold bias (Table 1) seen in Figure 3.

The monthly 2 m air temperature comparisons are shown in Figure 4. The air temperatures that are used are the blended product (described in section 2) that was then processed via the iterative function of *Launiainen and Vihma* [1990] to estimate the temperature at the calculation level, which is 2 m. This figure also shows that the iterative method produces some additional biases when comparing AIRS to the GC-Net data. At all three stations, the derived AIRS air temperatures are too high in the summer (~2.5 K) and winter months (~5 K). The RMSEs are about 1° larger than that for the skin temperatures (Table 1), although the monthly variations are still captured well with the AIRS data.

The final comparisons with GC-Net are done with the 2 m specific humidity produced from AIRS blended temperature and relative humidity products. When comparing this 2 m specific humidity product to the GC-Net station data (Figure 5 and Table 1), an average RMSE of 18.8% was found. At South Dome station, AIRS produces specific humidities that are consistently higher than those from the GC-Net in the summer, while at the other stations the differences are more varied. Overall, the winter specific humidity from AIRS is very consistent in magnitude to the GC-Net station measurements.

Air temperature comparisons with PROMICE in the ablation zones (Figure 6 and Table 1) are similar to those from the GC-Net station data, with winter and summer temperatures being slightly warmer from the AIRS than from the PROMICE station data. The largest discrepancies between AIRS and PROMICE data occur at the QAS_U and TAS_U stations in the summer months. This is most likely the result of the larger AIRS footprint, which has ice-free ocean contamination along these coastal areas of the ice sheet, and the larger

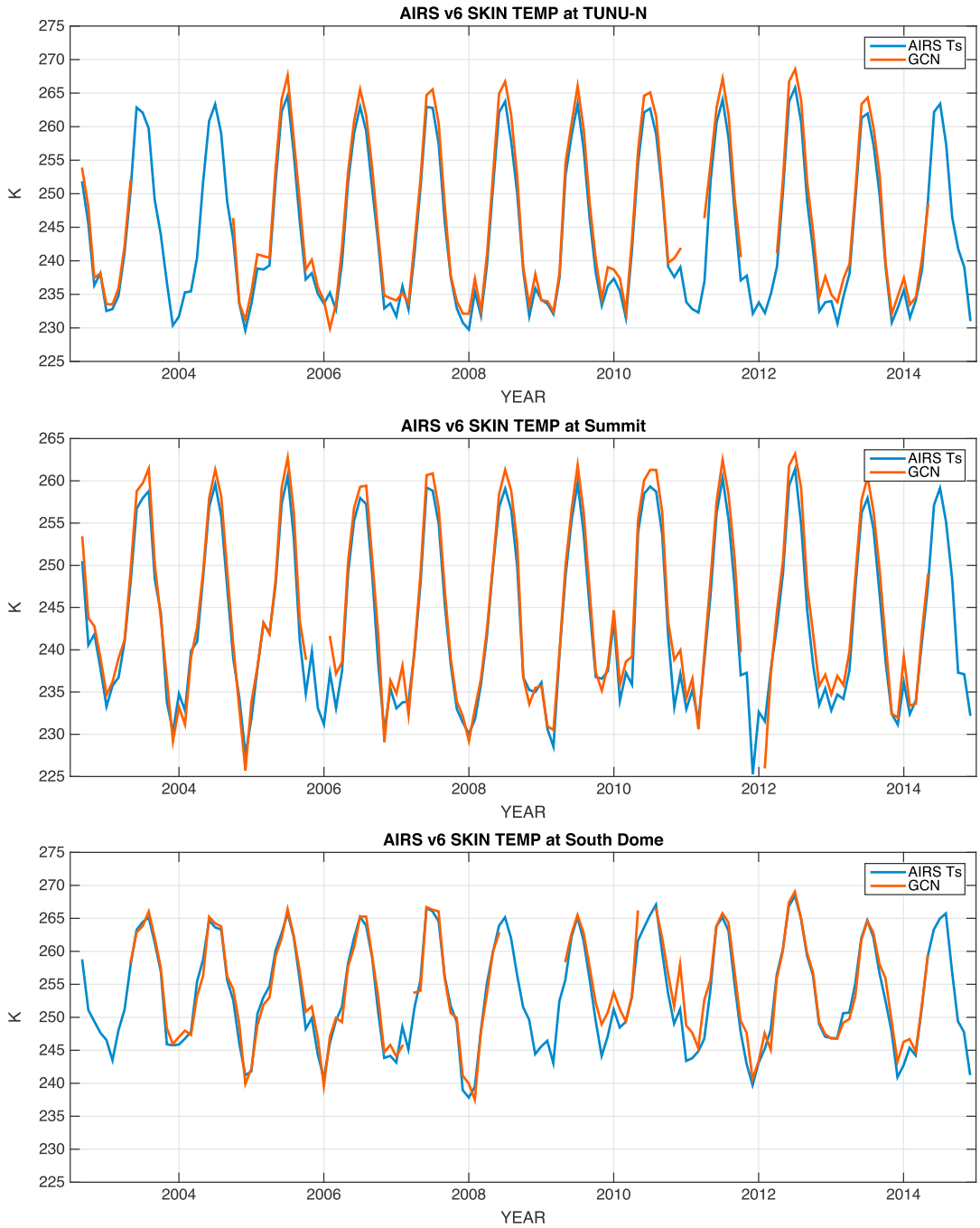

Figure 3. Comparison of monthly mean AIRS V6 skin temperatures with Automated Weather Stations (AWS) part of the GC-Net in Greenland for 2003–2014. Blue lines are AIRS and red lines are GC-Net. Locations of the AWS appear in Figure 1.

subgrid heterogeneity in this area compared to the accumulation zones. Thus, temperatures are much higher in the summer months from AIRS because the temperature of the nearby open water is much warmer. However, in the winter months the air temperatures between AIRS and these two stations are very similar. AIRS has the closest temperatures compared to the KPC_U and THU_U stations, which are on the northern portion of the ice sheet. At these stations, even though they are close to the coasts, there is less contamination due to water compared to the southern stations possibly due to the presence of sea ice even in the summer. At the KAN_M station, AIRS shows warmer summer and winter temperatures; however, the monthly variability is captured rather well.

Table 1. AIRS and GC-Net and PROMICE Comparisons

Variable	Station	Mean (AIRS)	Standard Deviation	Bias (AIRS-GC-Net)	RMS
Skin temperature (K)	Tunu-N	244.28	11.28	−1.75	2.01
	Summit	243.09	9.84	−1.40	2.00
	South Dome	253.39	8.01	−0.79	2.00
Air temperature (K)	Tunu-N	251.29	10.28	1.54	3.15
	Summit	248.85	9.86	3.01	3.26
	South Dome	257.00	8.16	2.68	3.01
	THU_U	263.16	8.80	1.98	2.20
	QAS_U	269.63	7.30	2.23	3.08
	KAN_M	264.37	7.67	2.59	2.94
	KPC_U	257.41	10.19	1.66	1.95
	TAS_U	269.26	5.61	−0.072	1.88
Specific humidity (g/kg)	Tunu-N	0.84	0.86	−0.107	0.067
	Summit	0.66	0.64	0.020	0.15
	South Dome	1.29	0.99	0.154	0.28
	THU_U	1.69	1.25	0.016	0.14
	QAS_U	2.57	1.70	0.126	0.79
	KAN_M	1.74	1.28	−0.053	0.21
	KPC_U	1.32	1.29	0.117	0.21
	TAS_U	2.01	0.91	−0.63	0.88

Specific humidity comparisons with PROMICE (Figure 7 and Table 1) show different results than those when AIRS was compared to GC-Net. When comparing AIRS with the southern stations (QAS_U and TAS_U), AIRS has a much higher specific humidity in the summer compared to QAS_U and a much lower specific humidity in the summer compared to TAS_U. AIRS RMSE values are large, with 0.88 g kg^{-1} for TAS_U and 0.79 g kg^{-1} for QAS_U, respectively. The results for specific humidity at the northern stations (THU_U and KPC_U) are consistent with those of temperature, where AIRS shows good agreement with the observations. The specific humidity from AIRS is also very similar to those from KAN_M.

It is important to keep in mind that these comparisons are done from a point measurement (GC-Net and PROMICE) to the nearest grid box on the 25 km^2 polar stereographic grid (AIRS), so we expect some variations to result from the spatial differences, especially along the coast of Greenland in the ablation zones. The ablation zone has very large subgrid heterogeneity due to dark snow, melt ponds, bare ice, and snow, especially in the summer months. This variability is smoothed out when using remotely sensed data with larger footprints and being in close proximity to the coasts, the addition of ice-free water will also impact the retrieval. This is why AIRS data products can be so different when compared to the PROMICE stations in the ablation zone, especially in the summer months. Except for the southern, coastal PROMICE stations (QAS_U and TAS_U), AIRS shows small RMSE (2.75°C and 0.18 g kg^{-1}) with GC-Net and PROMICE in both the accumulation and percolation zones.

Regardless of these spatial differences, we use the RMSEs found in the AIRS data (Table 1) to estimate the uncertainty of the BMF13 vapor flux product. Other factors causing errors in the flux are the uncertainties in the wind speed, air density, and the water vapor transfer coefficient. An error estimate of 0.8 m s^{-1} was chosen for the ERA-Interim wind speed following *Jakobson et al.* [2012]. The accuracy of the water vapor transfer coefficient is probably no better than ±20% [*Cronin et al.*, 2006]. The error of the air density was estimated from the errors in the air temperature from AIRS. Average values of the calculated sensitivities, estimated uncertainties, and the final uncertainties are shown in Table 2. If we assume that the variables are independent, the combined uncertainty of the GrIS vapor flux (σ_E) can be computed via

$$\sigma_E^x = \Sigma\sigma_x^2\left(\frac{\partial E}{\partial x}\right)^2 \tag{2}$$

where σ_x are the uncertainty of each variable in (1) and $\left(\frac{\partial E}{\partial x}\right)$ is the derivative of (1) with respect to each variable. Using (2), σ_E was found to be 5.79×10^{-3} kg m^{-2} d^{-1}, which corresponds to about a 34% uncertainty overall. However, if we also include the error introduced by the assumptions of the Monin-Obukhov similarity theory, which were found to be 10% for stable boundary layers [*Salesky and Chamecki*, 2012], then we get an overall error of ~44%. However, if we remove the QAS_U and TAS_U station RMSE,

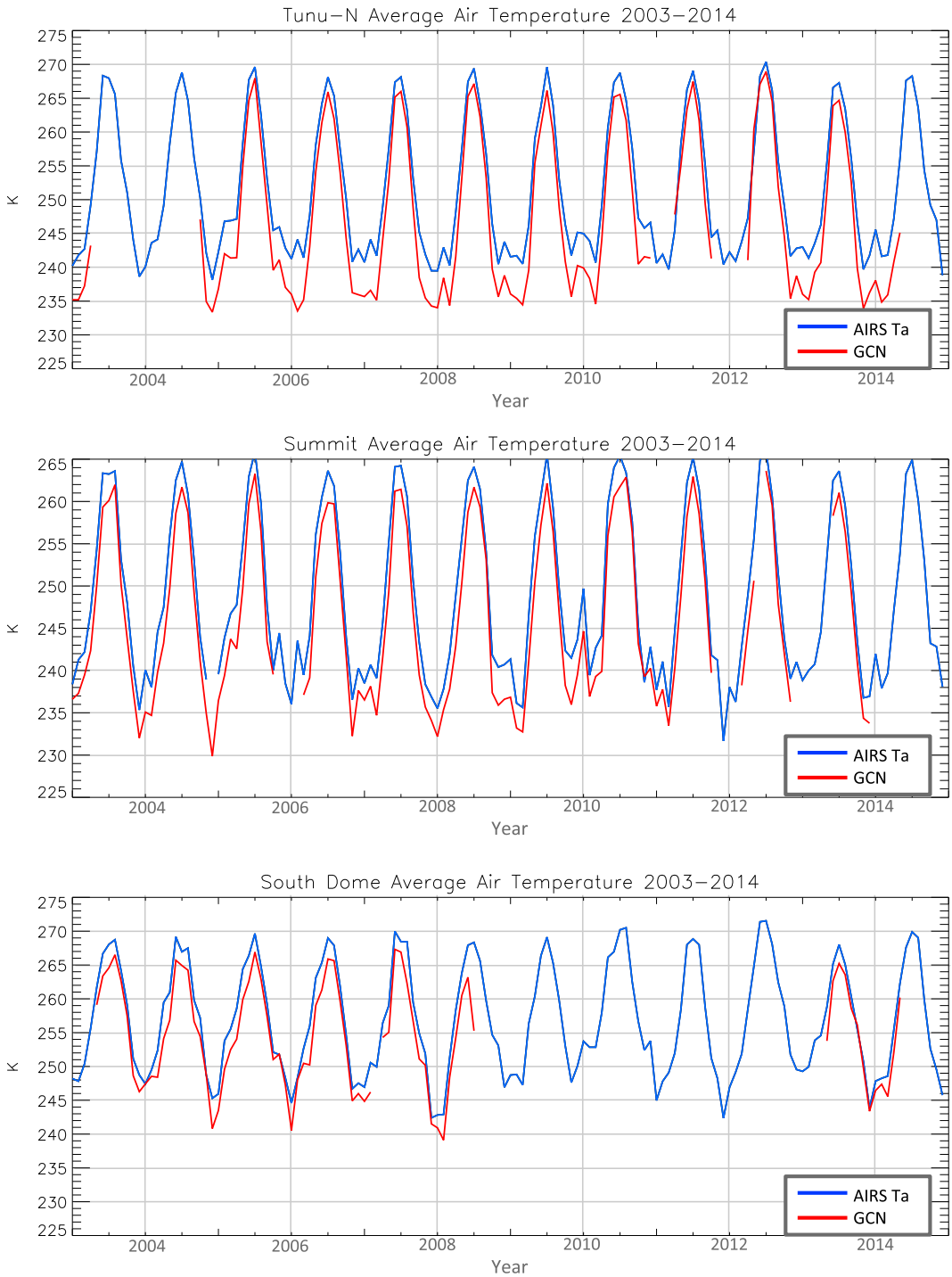

Figure 4. Monthly comparison of AIRS blended air temperature with Automated Weather Stations (AWS) part of the GC-Net in Greenland for 2003–2014. Black lines are AIRS and red lines are GC-Net. Locations of the AWS appear in Figure 1.

due to errors introduced by ocean contamination and the loss of the subgrid heterogeneity in the ablation zone due to the large AIRS footprint, we get an overall 15% uncertainty, which, combined with the similarity theory error, yields a total uncertainty of ~25%. This is a small error when compared to the range of variability in the GrIS flux during the 2003–2014 time period, and we assume that conclusions on the interannual and spatial variations are robust.

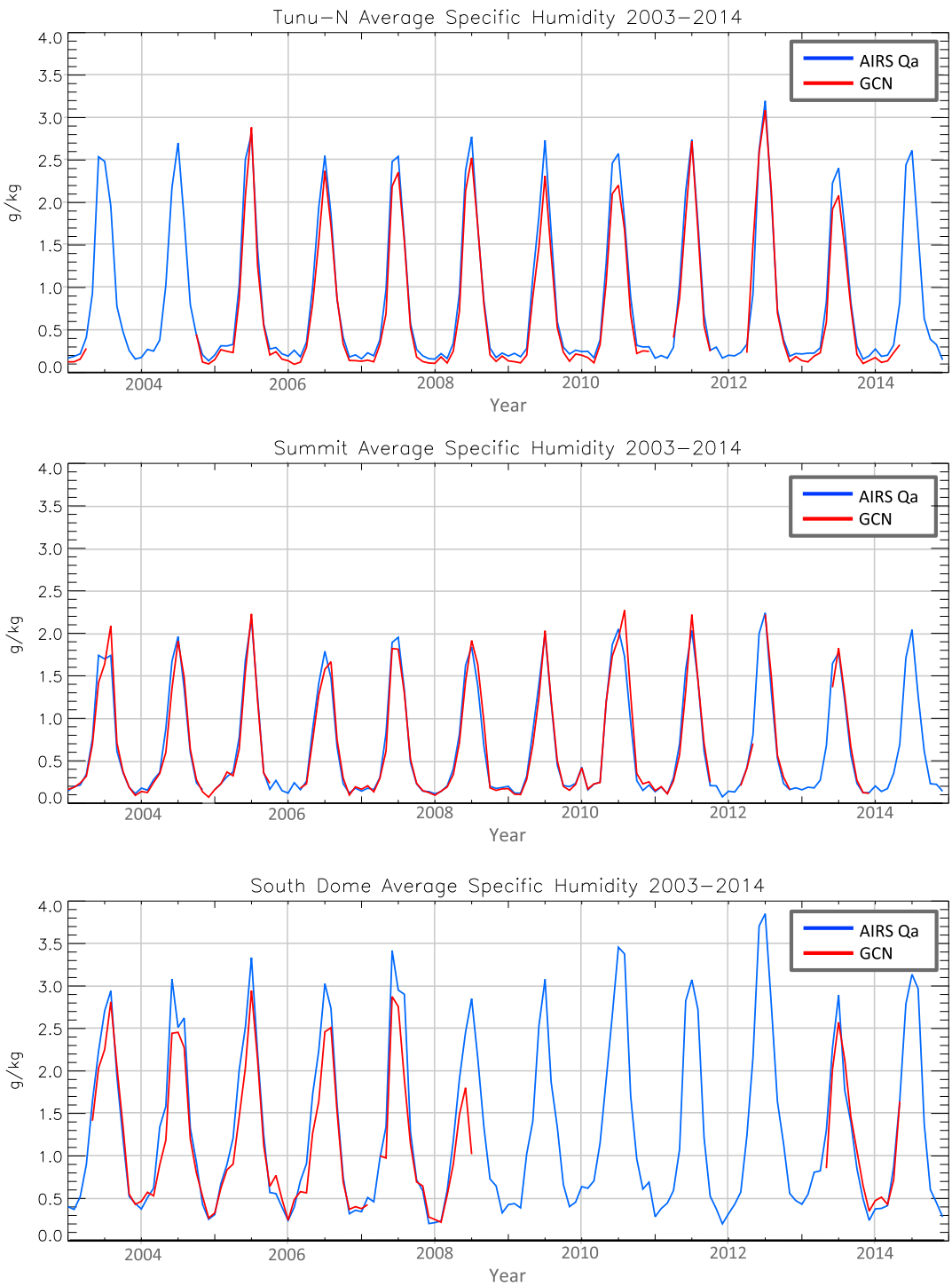

Figure 5. Monthly comparison of AIRS blended specific humidity with Automated Weather Stations (AWS) part of the GC-Net in Greenland for 2003–2014. Black is AIRS and red is GC-Net data. Locations of the AWS appear in Figure 1.

4. Results

4.1. BMF13 Sublimation/Deposition Climatology 2003–2014

The AIRS-derived vapor flux integrated over the GrIS follows a pronounced annual cycle, with the largest deposition occurring in the winter months and the strongest sublimation/evaporation occurring in the

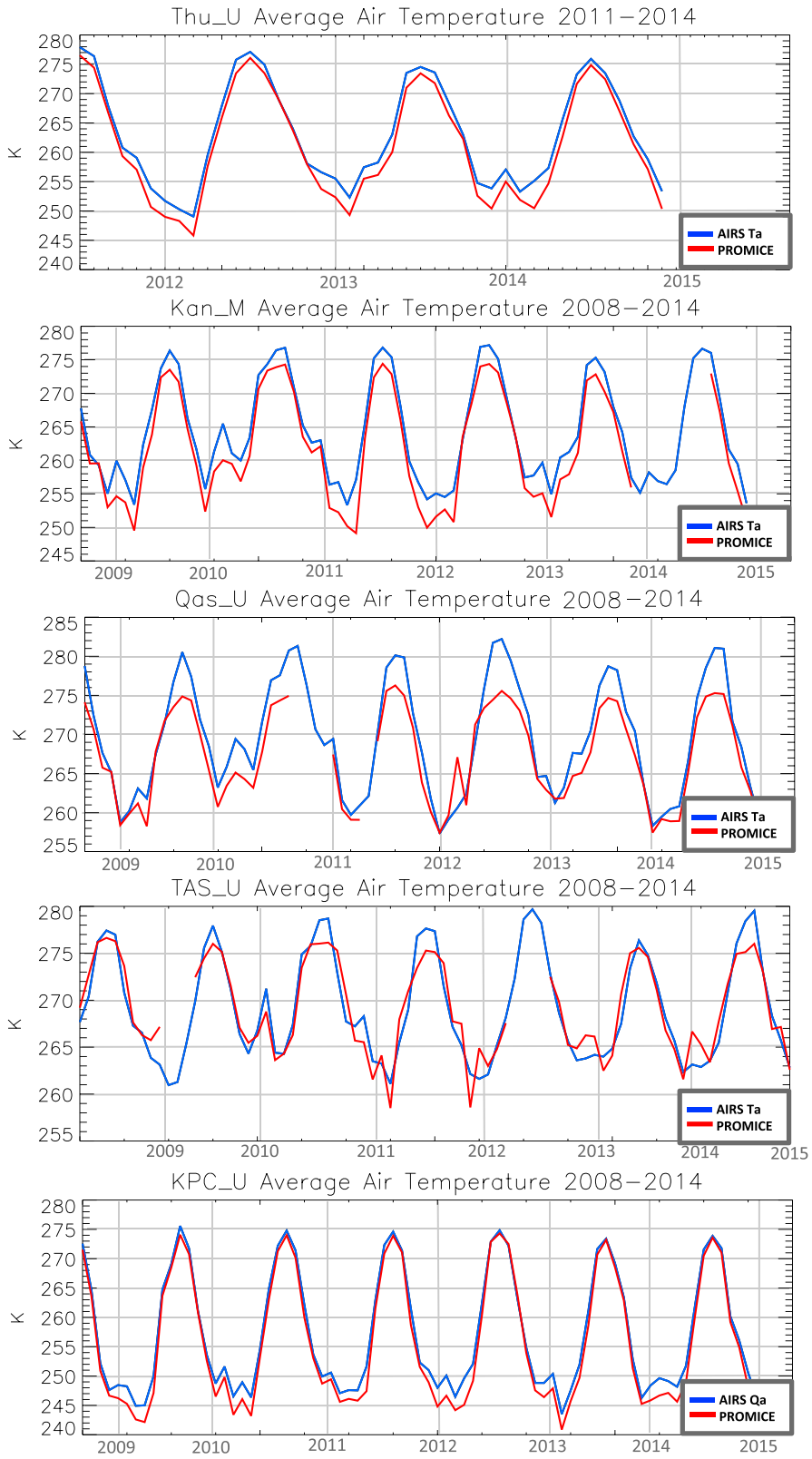

Figure 6. Monthly comparison of AIRS blended air temperature with Automated Weather Stations (AWS) part of PROMICE in Greenland. Blue lines are AIRS and red lines are PROMICE data. Data for THU_U begin in July 2011, KAN_M begin in September 2008, KPC_U and QAS_U begin in August 2008, and TAS_U begin in April 2008. Locations of the AWS appear in Figure 1.

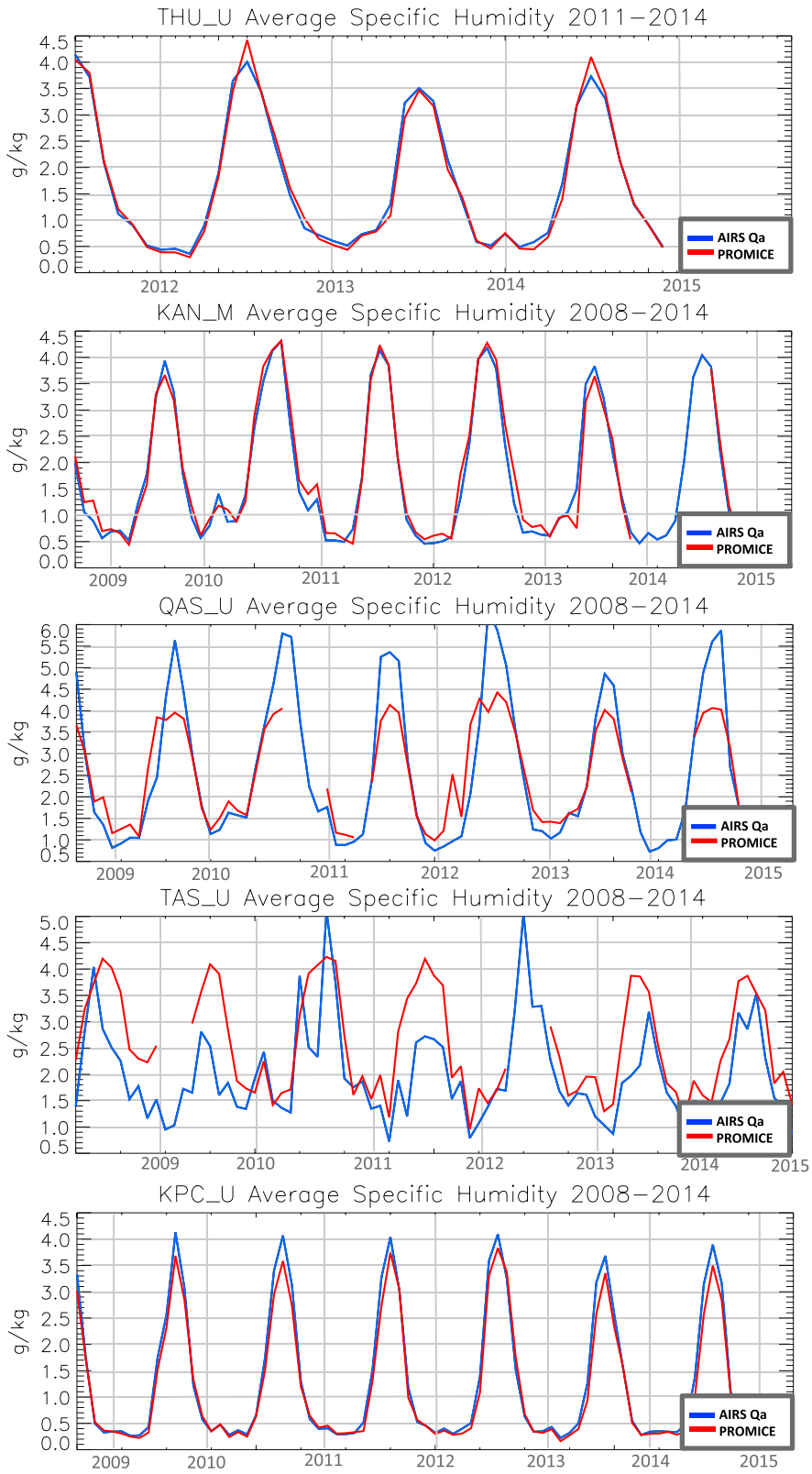

Figure 7. Monthly comparison of AIRS blended specific humidity with Automated Weather Stations (AWS) part of PROMICE in Greenland. Blue lines are AIRS and red lines are PROMICE data. Data for THU_U begin in July 2011, KAN_M begin in September 2008, KPC_U and QAS_U begin in August 2008, and TAS_U begin in April 2008. Locations of the AWS appear in Figure 1.

Table 2. Sensitivity of the Sublimation/Deposition to Different Input Uncertainties Expressed as Percentages

Variable (X)	$(dE/dx)^2$	$(\sigma_x)^2$	$(\sigma_x)^2(dE/dx)^2$
ρ (kg/m^3)	1.27×10^{-1}	0.034	4.32×10^{-3}
C_{Ez} (−)	110,649	9.0×10^{-8}	9.96×10^{-3}
S_r (m/d)	1.33×10^{-12}	2.69×10^{9}	3.57×10^{-3}
$q_{s,i}$ (kg/kg)	823,012	1.0×10^{-8}	2.38×10^{-2}
q_z (kg/kg)	823,012	4.18×10^{-8}	3.44×10^{-2}
σ_E (kg m^{-2} d^{-1})	5.79×10^{-3}		
$<E>$ (kg m^{-2} d^{-1})	0.017		

summer months, peaking in July (Figure 8). The largest interannual variability in the vapor flux occurs during the summer months spanning 0.067 Gt d^{-1}, and the smallest range in the vapor flux occurs in the winter months spanning 0.020 Gt d^{-1} (Figure 8). This is because in the summer the skin temperatures exhibit the smallest year-to-year variations, but the 2 m specific humidity shows the largest variations (Figure 9); thus, the vapor flux will have the largest change in magnitude. The opposite is true for winter, when the skin temperatures have the largest variations and the 2 m specific humidities show the smallest variations. Although the opposite is seen in the winter, the magnitude of the differences between the 2 m and surface specific humidity is much smaller than in summer, and the positive vapor flux is about 5 times the magnitude of the deposition. The largest vapor flux deviation from the average occurs in the elevations between 0.3 km and 1.5 km (near the edge of the ice sheet), and smaller deviations occur at higher elevations. The locations near the ice sheet edge are the most susceptible to atmospheric influences from the surrounding water.

Since the largest variability in the vapor flux occurs in July, anomalies for the entire Greenland ice sheet and drainage basins (Figure 1a) are shown for this month in Figure 10. For the entire ice sheet positive anomalies in the vapor flux occur in 2003, 2009, 2010, and 2012. This is consistent with the larger surface melt events in the past decade [*Andersen et al.*, 2015], where July skin temperature anomalies are positive (Figure 10). Large negative anomalies occur in 2005, 2006, 2011, 2013, and 2014. There is no statistically significant trend in the vapor flux in July or annually during the period between 2003 and 2014. During positive anomaly vapor flux years, the relative humidity is almost always below average (except for 2003), and skin temperatures almost always show larger positive anomalies than the air temperatures (except for 2009). Positive relative humidity anomalies are seen during years with negative vapor flux anomalies and lower skin/air temperatures.

Baffin Bay and Greenland Sea (northern regions) have similar July temperature and relative humidity anomalies, but do not show the same vapor flux anomalies. However, both of these regions show positive anomalies

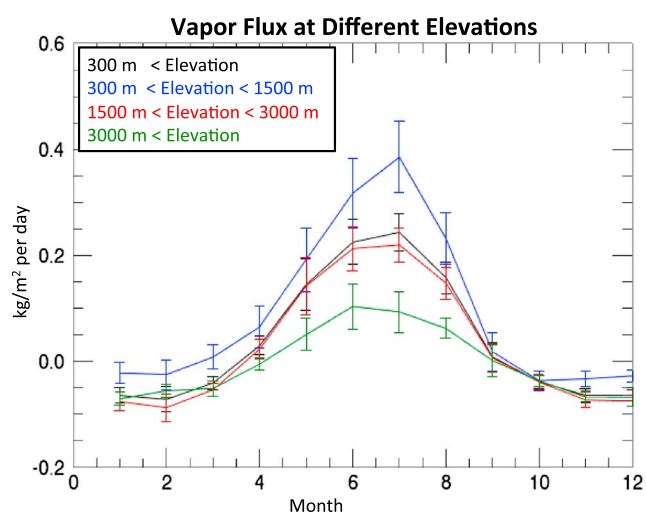

Figure 8. Average (2003–2014) monthly BMF13 vapor flux for the entire Greenland ice sheet at different elevations. The black line is for all elevations higher than 300 m above sea level (asl), blue is for all elevations between 300 m and 1500 m asl, red is for all elevations between 1500 m and 3000 m asl, and green is for elevations greater than 3000 m asl. Standard deviations are shown as the error bars.

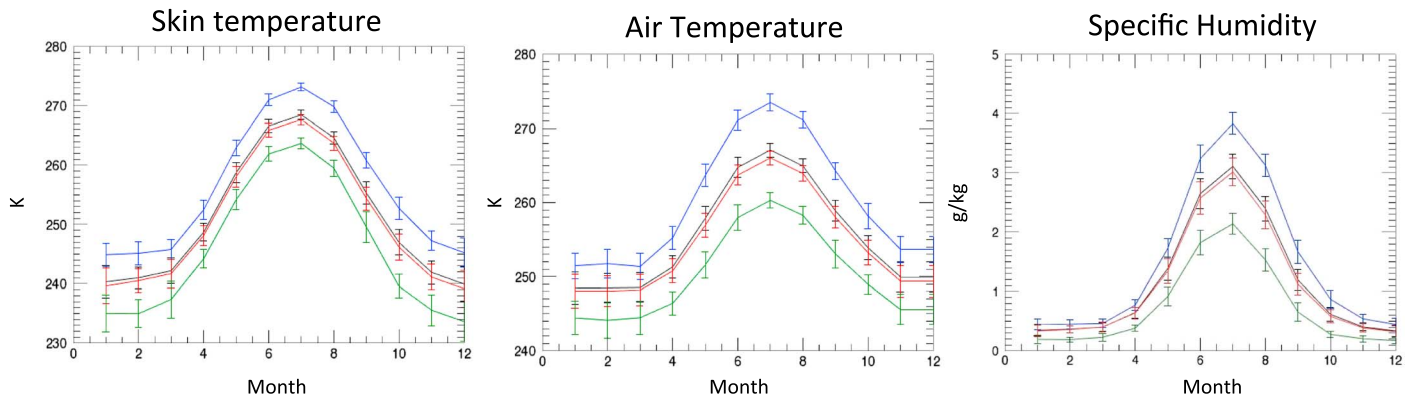

Figure 9. Average (2003–2014) monthly (left) skin temperature, (middle) air temperature, and (right) specific humidity for the entire Greenland ice sheet at different elevations. The black line is for all elevations higher than 300 m asl, blue is for all elevations between 300 m and 1500 m asl, red is for all elevations between 1500 m and 3000 m asl, and green is for elevations greater than 3000 m asl. Standard deviations are shown as the error bars.

in 2010 and 2012 (Figure 10), the two years with the highest surface melt. Since 2009, the Baffin Bay and Greenland Sea areas have seen a dramatic increase in relative humidity and subsequently a decrease in the vapor flux. These increases in relative humidity could be due to a more frequent presence of clouds or could be caused by a decrease in sea ice coverage in the surrounding seas leading to more evaporation [*Boisvert et al*., 2015b].

On the southern tip of the ice sheet, the Davis Strait and the North Atlantic regions show similar atmospheric anomalies but divergent vapor flux anomalies, similar to the northern regions (Figure 10). However, no positive relative humidity trends are seen; instead, each year changes from positive anomalies to negative anomalies the next year. These regions have seen increased skin and air temperature between 2003 and 2012. Since these regions are lower in elevation and latitude, they see surface melt each year, and thus vapor flux anomalies in 2010 and 2012 are minimal compared to the northern regions, where surface melt is observed less frequently.

4.2. Case Study: Comparing July 2012 and July 2013

There is a stark contrast between a high surface melt year, 2012, and an average surface melt year, 2013 (Figures 11 and 12). In July 2012 there was 0.88 Gt more mass lost by the vapor flux than the average (2003–2014), and 1.53 Gt more than in 2013. This can be seen in Figure 11, where in 2012 a larger positive vapor flux is occurring along the ice edge and at higher elevations compared to 2013. In 2013 there was more snowfall and less mass loss to sublimation than in 2012, and this helped contribute to a smaller mass loss of the ice sheet in 2013 compared to 2012. Figure 12 shows the daily vapor flux from GrIS for July 2012, July 2013, and July 2003–2014. The vapor flux in 2013 was very similar to the 2003–2014 average, but the 2012 vapor flux produced three high-sublimation spikes around 12, 22, and 29 July. These are consistent with the findings from *Nghiem et al*. [2012], who showed concurrent large melt events covering the majority of the ice sheet on 12 and 29 July. They also note that normal melt rates occurred on 8 July, and Figure 12 shows that around 8 July 2012, the vapor flux is consistent with the average 2003–2014. Shortly, after the 12 July melt event, colder weather reduced the melt extent back to normal levels. Colder conditions also reduce the 2012 vapor flux in Figure 12 after the peak on 12 July.

In July 2012 there was a high amount of clouds over GrIS, especially in the area around Summit, but unlike other years these clouds were low level, comprised of liquid water droplets, and were optically thin [*Bennartz et al*., 2013]. This combination allowed for solar radiation to still reach the surface, while allowing increased downwelling longwave radiation at the surface [*Bennartz et al*., 2013]. These two effects caused warmer temperatures across the entire ice sheet. This is also shown in Figure 10. Northern regions saw about 1 K positive temperature anomalies, whereas the southern regions saw a 2 K positive anomaly. However, *Neff et al*. [2014] also attribute the 2012 melt event to water vapor transported to the ice sheet via atmospheric rivers and warm ocean waters south of Greenland. This increase in water vapor is evident in Figure 10 for the Davis Strait and N Atlantic regions, showing high relative humidities in 2012 compared to 2013. In July

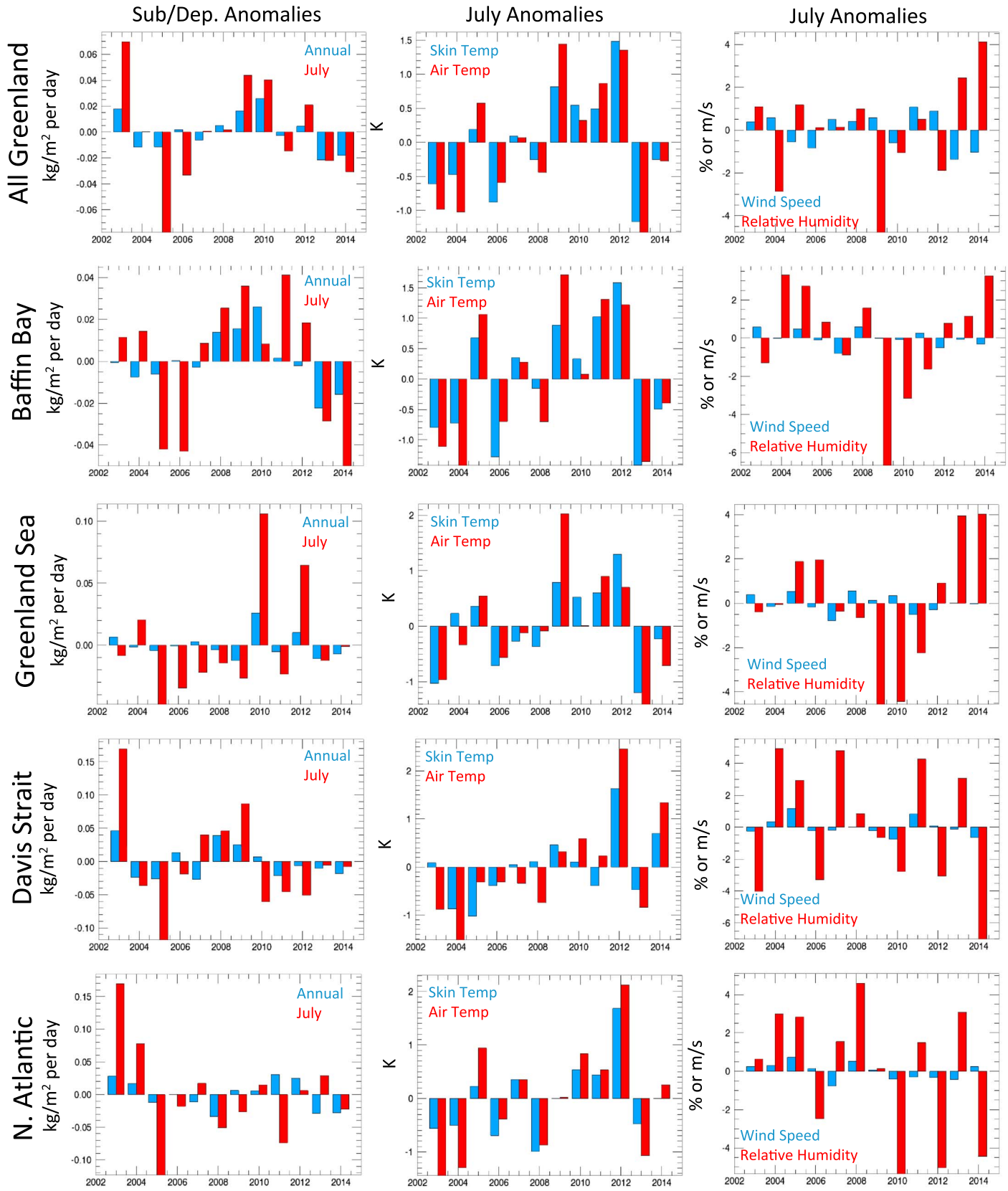

Figure 10. (left column) Vapor flux anomalies annually and for July, (middle column) July skin and air temperature anomalies, and (right column) July wind speed and relative humidity anomalies for the entire Greenland ice sheet and the regions shown in Figure 1.

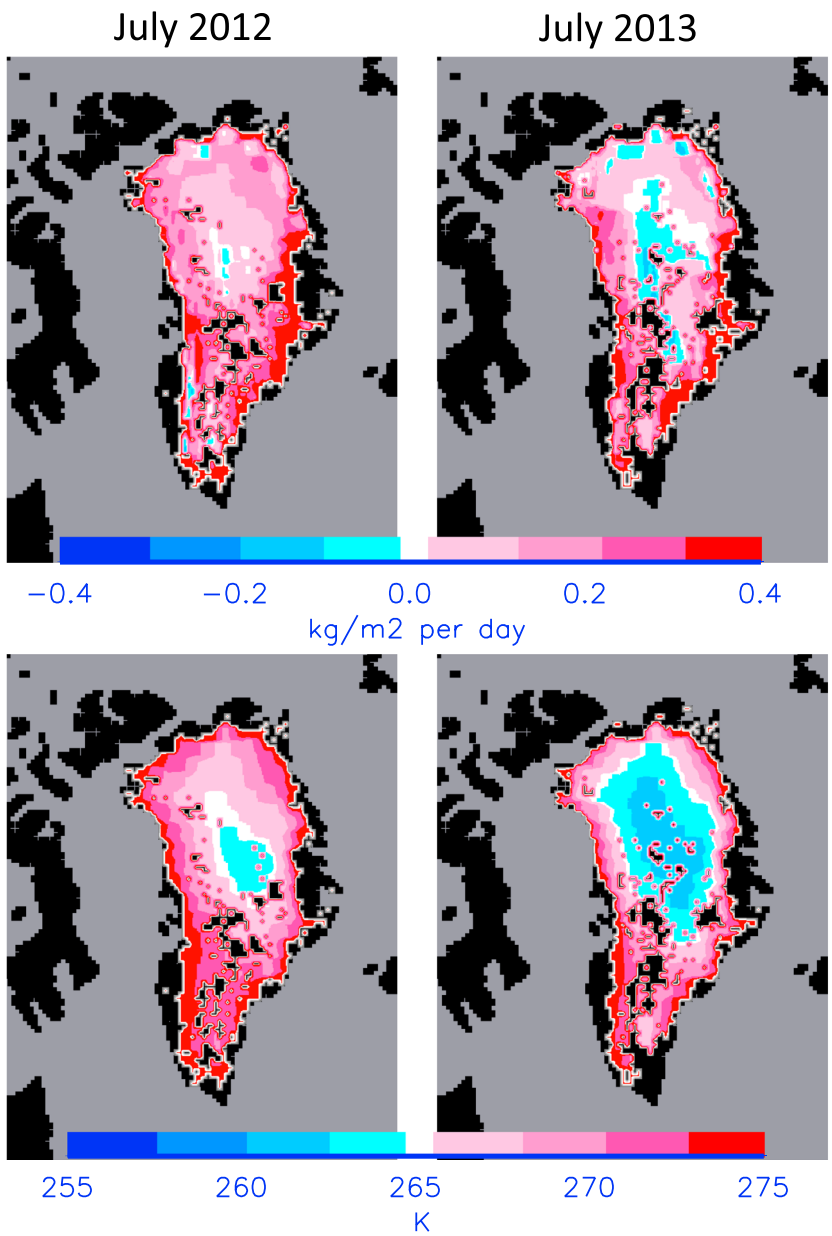

Figure 11. (top) High vapor flux July (2012) versus normal vapor flux July (2013). (bottom) The July 2012 skin temperature versus the July 2013 skin temperature. Black is land/no data, and grey is water.

2012, unlike 2013, more low-level clouds over Summit and northern areas, along with increased water vapor from lower latitudes initiated melt over the majority of the ice sheet. This in turn produced high levels of evaporation from melt ponds and sublimation from the snow/ice surface compared to July 2013, which witnessed different atmospheric conditions and normal melt conditions.

4.3. Comparison With RACMO2.3

We begin by looking at the averaged daily vapor flux integrated over the entire ice sheet (elevations greater than 300 m above sea level (asl)) for the period 2003–2014 (Figure 13 and Table 3). RACMO2.3 (red line) and BMF13 (black line) are similar in shape and magnitude of the annual cycle, except in June–July where the magnitude of RACMO2.3 sublimation is larger than BMF13. For both data sets, there are small amounts of deposition in the winter months, with sublimation occurring the rest of the year, peaking in July. There are

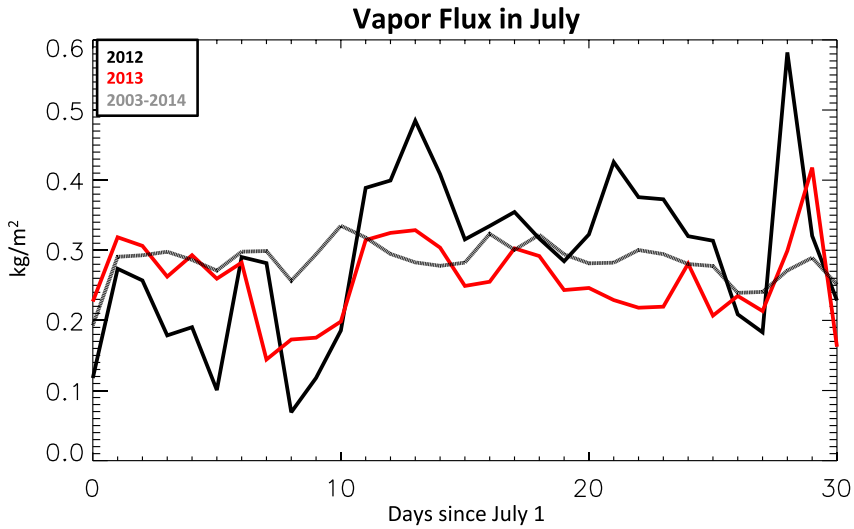

Figure 12. Daily GrIS vapor flux beginning on 1 July for years 2012 (black line), 2013 (red line), and the 2003–2014 average (grey line).

differences in the magnitudes of the vapor flux between the models. For example, the wintertime deposition is slightly stronger in BMF13 and the peak in sublimation in July is smaller than in RACMO2.3.

When the vapor flux is averaged over the entire year, BMF13 and RACMO2.3 differ by an average 7.1 Gt yr^{-1} (Table 4). These differences arise due to the larger flux in the summer months from RACMO2.3, producing fluxes that are 0.05 Gt d^{-1} larger than in BMF13. These differences are witnessed at elevations between 1500 and 3000 m asl, where BMF13 shows slight deposition, due in part to lower skin temperatures and higher specific humidity from AIRS (see Figure 16). This causes the flux to be slightly negative, which creates an overall average in June and July to be smaller than that from RACMO2.3, which shows a positive vapor flux over the entire ice sheet. In the winter months, similar amount of deposition occurs in BMF13 and RACMO2.3, with averages of −0.18 and −0.17 Gt d^{-1}, respectively (Figure 13). During the transition months (spring and fall) the vapor flux from BMF13 only differs by 0.05 Gt d^{-1} (spring, MAM) and 5.4×10^{-3} Gt d^{-1} (fall, SON) from RACMO2.3 (Figure 13). Taking the average loss of mass for 2003–2014 due to the vapor flux, we found 14.9 Gt yr^{-1} and 22.0 Gt yr^{-1} for BMF13 and RACMO2.3, respectively. These estimates are in line with the vapor flux estimates made by *Lenaerts et al.* [2012] for years 1960–2011.

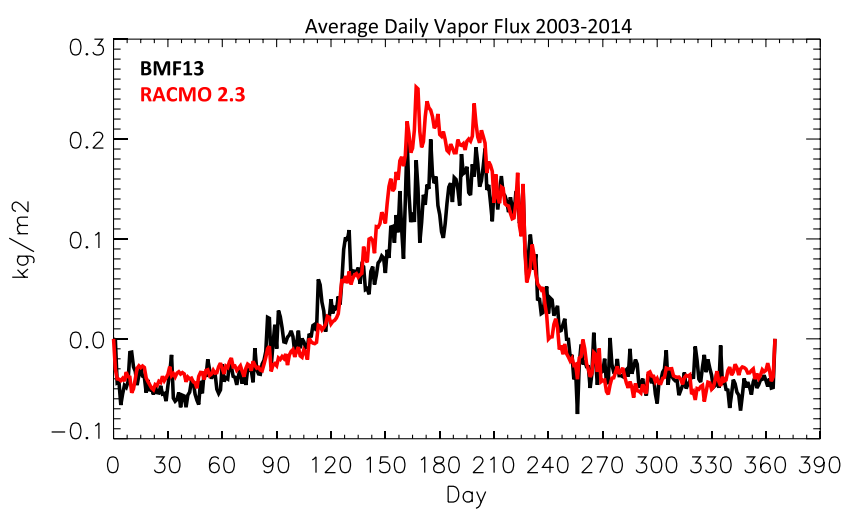

Figure 13. Average daily vapor flux comparison for 2003–2014. Black is BMF13 and red is RACMO2.3. Values are averages for all locations on the Greenland ice sheet that are at an elevation of 0.3 km or higher.

Table 3. Average Vapor Flux for 2003–2014 (kg/m^2/d) for BMF13 and RACMO2.3

Month	BMF13	RACMO2.3	Difference
January	−0.043	−0.039	−0.004
February	−0.049	−0.036	−0.013
March	−0.026	−0.027	0.001
April	0.011	−0.006	0.017
May	0.066	0.075	−0.009
June	0.133	0.199	−0.066
July	0.153	0.190	−0.037
August	0.093	0.087	0.006
September	−0.018	−0.022	0.004
October	−0.036	−0.042	0.006
November	−0.037	−0.043	0.006
December	−0.047	−0.034	−0.013

The vapor flux differences vary across ice sheet elevations (Figure 14 and Table 4), with the largest differences occurring in the summertime. At the lowest elevations (between 300 m asl and 1500 m asl), along the edges of the ice sheet, annual vapor fluxes are very close, differing by only 1.9×10^{-3} Gt d^{-1}, with the largest differences occurring in the summertime. The deposition rates from both models at this elevation are very close to zero. At elevations between 1500 and 3000 m asl, comprising the majority of the ice sheet, the RACMO2.3 vapor flux is slightly larger than the BMF13 on an annual basis. During summer, sublimation rates were 3.05×10^{-2} Gt d^{-1} larger in RACMO2.3 and deposition rates 1.15×10^{-2} Gt d^{-1} less than BMF13 in the winter. At elevations greater than 3000 m asl, the annual vapor flux is close to zero, with BMF13 being slightly positive and RAMCO2.3 being slightly negative. This is mostly due to the larger sublimation from BMF13 in the summer months, where sublimation turns to deposition earlier (around the end of August) in RACMO2.3. In BMF13 this transition is slower. The opposite is seen in the spring when deposition changes to sublimation.

The largest differences in the summertime vapor flux (sublimation) occur at elevations between 1500 and 3000 m asl, with smaller differences at the other elevations. During the summer, at all elevations except for those greater than 3000 m asl, the sublimation rates from BMF13 are smaller than that from RACMO2.3. In the winter months the deposition rates are nearly identical between the two data sets. All in all, the largest differences between the two data sets are seen between June and July at elevations less than 3000 m asl.

Along with elevation differences in the vapor flux, differences in each of the eight drainage basins outlined by *Wouters et al*. [2008] (shown in Figure 1c) were analyzed in order to understand the vapor flux in both accumulation and ablation areas. Figure 15 and Table 5 show these results. Here we found that the northern half of GrIS (regions 1, 2, 7, and 8) vapor flux is very similar for both RACMO2.3 and BMF13. The regions at the southern end of GrIS (3–6) show larger discrepancies. The vapor fluxes in these regions during the winter are very similar in the two products, but in summer BMF13 is higher (roughly double) than RACMO2.3 values. This is similar to the temporally averaged seasonal vapor fluxes for 2003–2014 shown in Figure 16. The region

Table 4. Average Yearly, Summer (Days 121–273), and Winter (Days 1–120, 274–365) Sublimation/Deposition for 2003–2014 From BMF13, RACMO2.3 for Different Elevations[a]

		BMF13	RACMO2.3	Difference
Annual	Elev > 0.3 km	0.017	0.026	−0.009
	1.5 > Elev > 0.3 km	0.045	0.047	−0.002
	3 > Elev > 1.5 km	0.011	0.022	−0.011
	Elev > 3 km	0.005	−0.002	0.007
Winter	Elev > 0.3 km	−0.077	−0.073	−0.004
	1.5 > Elev > 0.3 km	−0.025	−0.038	0.013
	3 > Elev > 1.5 km	−0.095	−0.086	−0.009
	Elev > 3 km	−0.087	−0.086	−0.001
Summer	Elev > 0.3 km	0.086	0.106	−0.02
	1.5 > Elev > 0.3 km	0.114	0.128	−0.014
	3 > Elev > 1.5 km	0.082	0.106	−0.024
	Elev > 3 km	0.063	0.048	0.015

[a]All values are in kg m^{-2} d^{-1}.

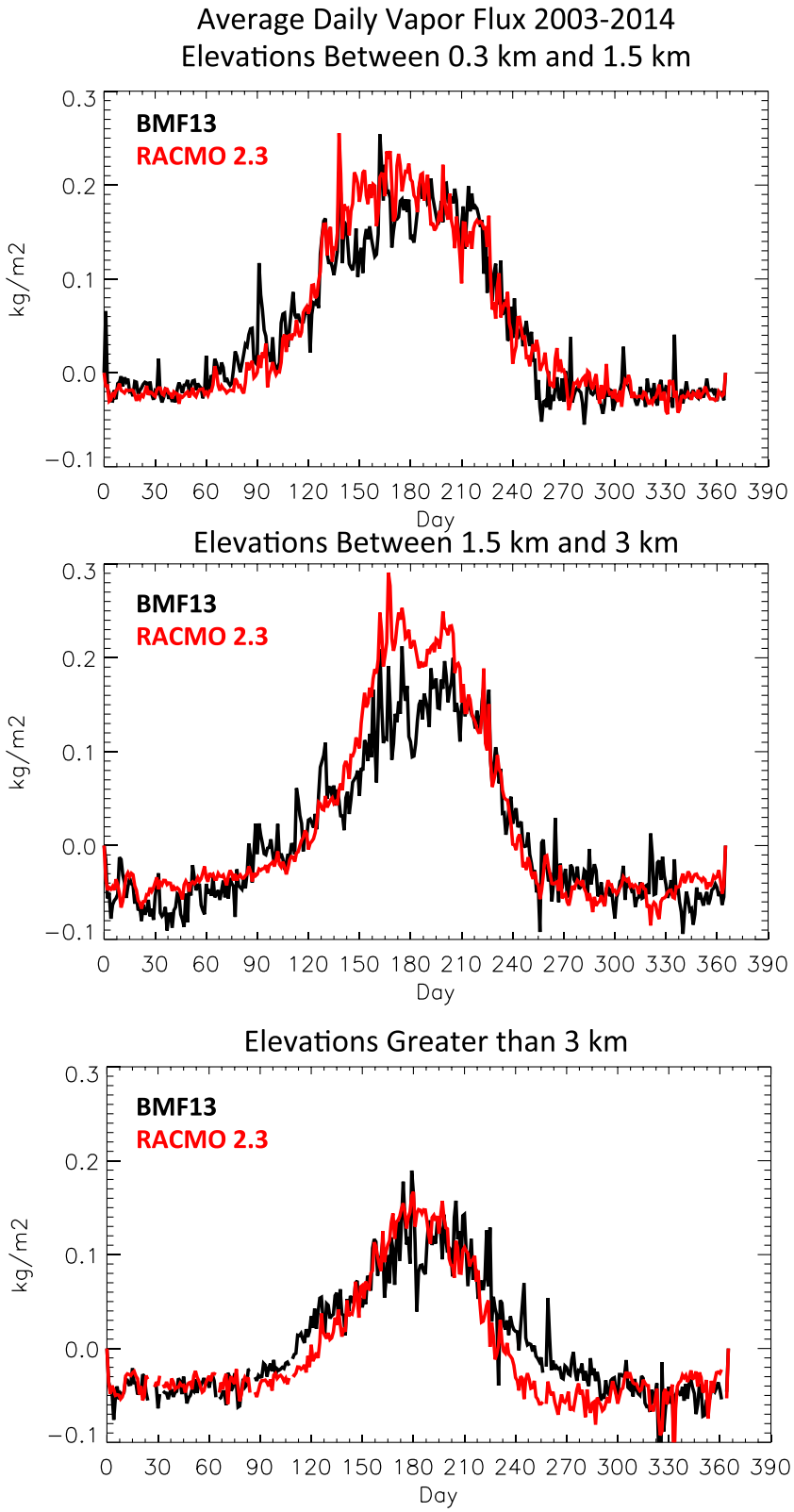

Figure 14. Average daily vapor flux comparison for 2003–2014 at different elevations. (top) Elevations between 0.3 and 1.5 km, (middle) elevations between 1.5 and 3 km, and (bottom) elevations greater than 3 km. The black lines are BMF13 and the red lines are RACMO2.3.

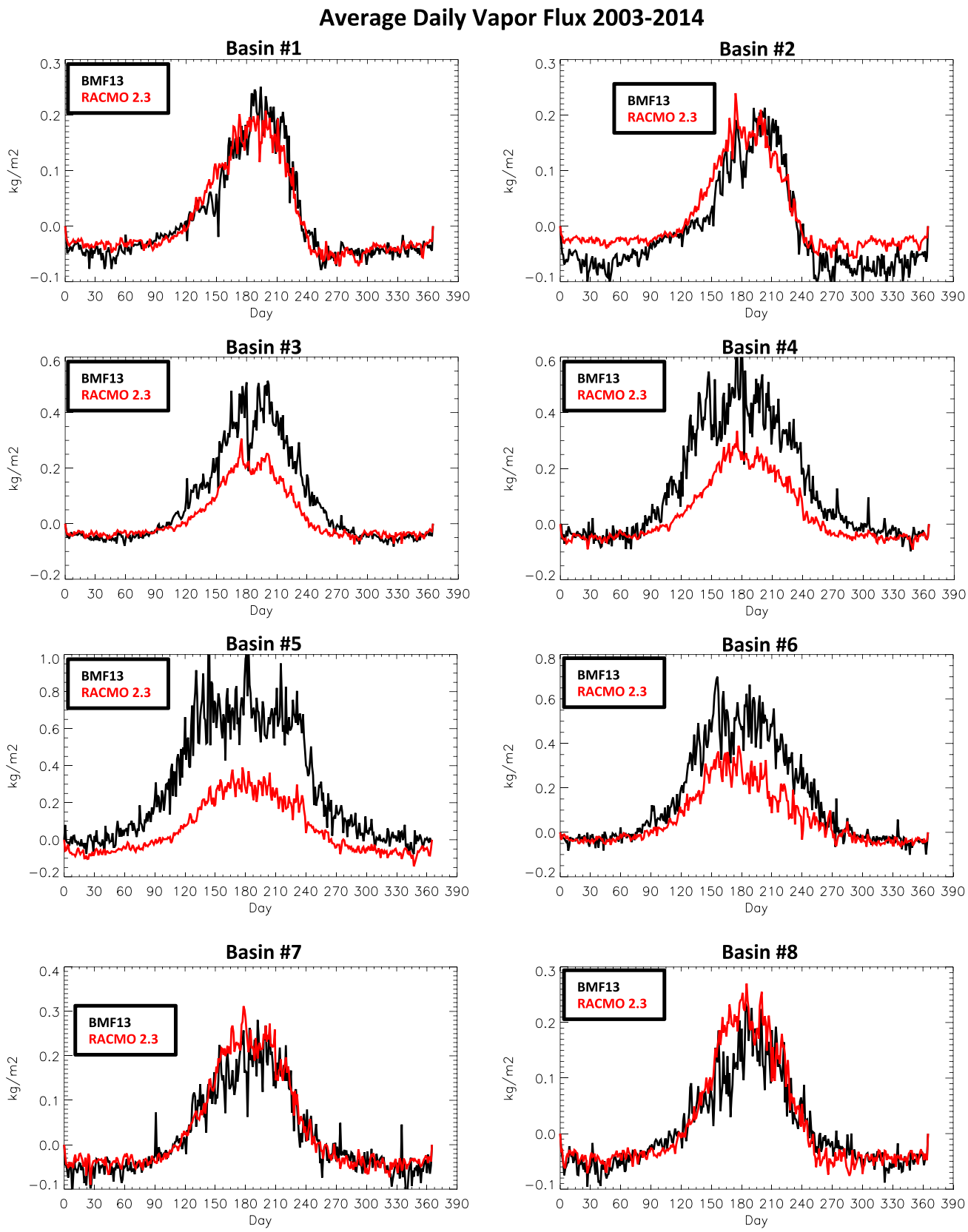

Figure 15. Average (2003–2014) daily vapor flux for the eight drainage basins [*Wouters et al.*, 2008] shown in Figure 1c. In each graph the red line represents RACMO2.3 and the black line represents BMF13.

Table 5. Average Yearly, Summer (Days 121–273), and Winter (Days 1–120, 274–365) Sublimation/Deposition for 2003–2014 From BMF13, RACMO2.3 for the 8 Drainage Basins Defined in Figure 1c[a]

	Region	BMF13	RACMO2.3	Difference
Annual	1	0.010	0.011	−0.001
	2	−0.011	0.015	−0.026
	3	0.075	0.022	0.053
	4	0.126	0.034	0.092
	5	0.284	0.052	0.232
	6	0.148	0.060	0.088
	7	0.020	0.032	−0.012
	8	0.008	0.017	−0.009
Winter	1	−0.039	−0.035	−0.004
	2	−0.060	−0.027	−0.033
	3	−0.038	−0.035	0.003
	4	−0.011	−0.040	0.029
	5	0.065	−0.049	0.114
	6	−0.007	−0.023	0.016
	7	−0.043	−0.037	−0.006
	8	−0.043	−0.042	−0.001
Summer	1	0.077	0.073	0.004
	2	0.054	0.072	−0.018
	3	0.230	0.100	0.130
	4	0.314	0.136	0.178
	5	0.578	0.189	0.389
	6	0.359	0.173	0.186
	7	0.108	0.126	−0.018
	8	0.077	0.097	−0.020

[a]All values are in kg m^{-2} d^{-1}.

with the largest discrepancies between the vapor flux products annually is region 5 along the southeast coast and, conversely, the regions with the smallest annual differences are regions 1 and 8 along the northwest side of the ice sheet. In Figure 16, along the southern and eastern edges of the ice sheet in March-April-May (MAM) and summer (June-July-August, JJA), BMF13 produces higher sublimation rates. In MAM, the area of deposition in RACMO2.3 is confined to a smaller area in the northern part of the ice sheet compared to BMF13. In JJA, RACMO2.3 shows sublimation over the entire ice sheet, whereas the BMF13 model produces a small amount of deposition at higher elevations (between 1500 and 3000 m asl) over the central ice sheet. In September-October-November (SON) and December-January-February (DJF), the magnitude of deposition is similar except for a few areas of larger deposition rates in the BMF13 product along the southern edge of the ice sheet.

One factor causing the differences in the two vapor flux products is the inclusion of the MISR roughness product in spring/summer months, and the largest differences between the models occurs where the roughest ice lies along the edge of the ice sheet, especially on the southwest region (see Figure 1d). Another factor could be due to the erroneous atmospheric variables from AIRS in the southeast region of GrIS. It appears that AIRS reports much higher temperatures compared to RACMO2.3 (Figure 17) and the PROMICE station QAS_U and TAS_U data (Figure 6) in the summer months, which account partially for these differences. Erroneous skin temperatures from AIRS are most likely due to the rapidly changing surface type near the ice edge and the proximity to the North Atlantic ice-free oceans, where there is likely some contamination in the larger footprint of AIRS compared to RACMO2.3. Regions 1 and 8, with the smallest differences between models, are not affected by warm ocean waters contaminating the AIRS footprint and have larger area over the more uniform ice sheet. Factors driving these differences will be discussed in the following section.

5. Discussion

5.1. Model Differences

Differences seen in the vapor flux between the two models can be explained by differences in model physics as well as differences in the data used to force the models. As mentioned earlier, RACMO2.3 also estimates drifting snow sublimation. When drifting snow sublimation is activated, surface deposition is assumed to

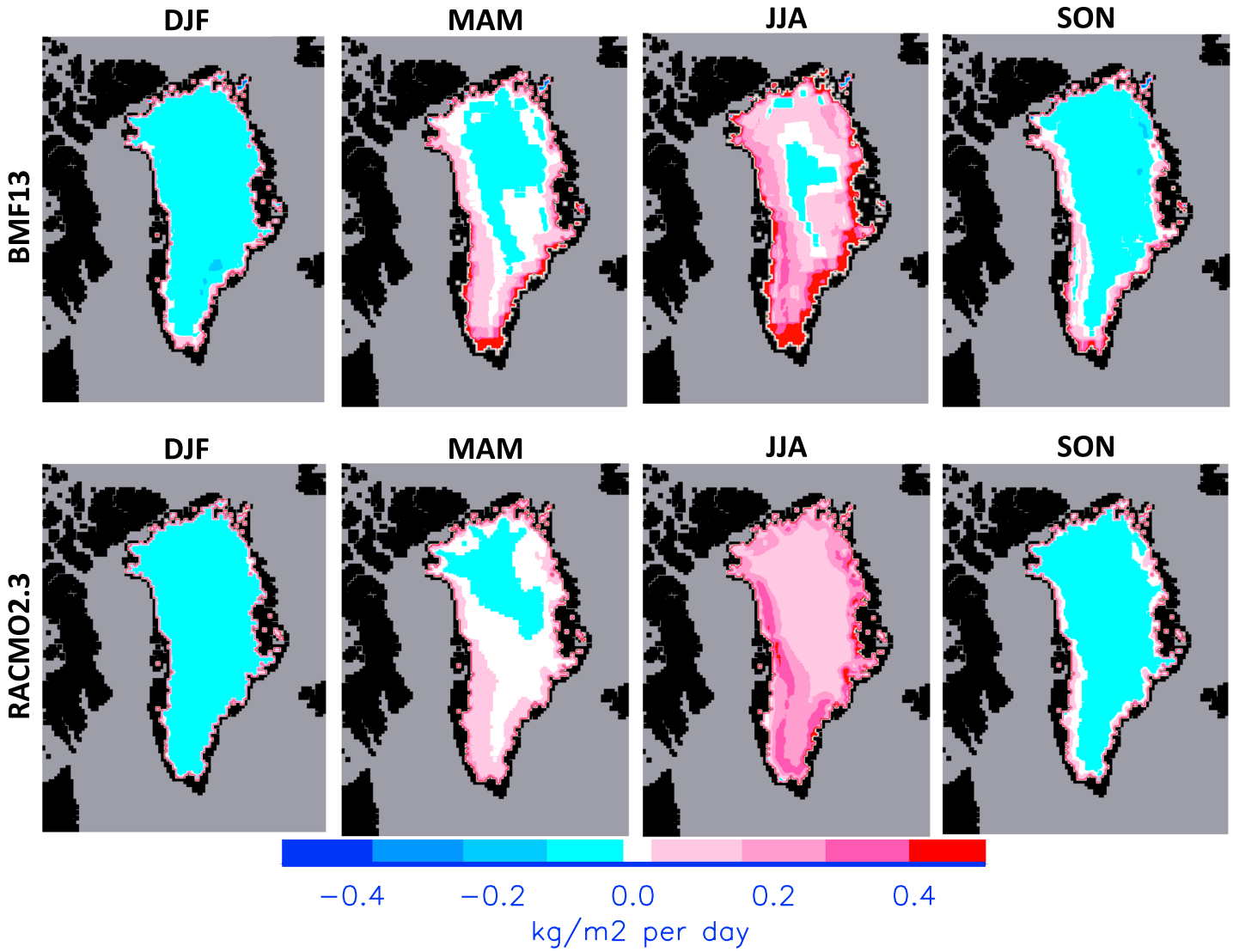

Figure 16. Average seasonal 2003–2014 vapor flux for (top row) BMF13, and (bottom row) RACMO2.3. Black is land with no ice or land that is not Greenland, and grey is no data.

be zero, following the reasoning that the surface air layer is quickly saturated and well mixed under strong wind conditions (no vertical temperature gradient). Since drifting snow occurs most often in the winter months and most frequently at lower elevations [*Lenaerts et al.*, 2012], we compared the outcome of both models using only included vapor flux data when there was no drifting snow sublimation to allow for the most robust comparison.

Although both models use Monin-Obukov similarity theory to estimate the vapor flux, some differences in the model physics between BMF13 and RACMO2.3 can be identified. For example, in the winter months, mostly stable boundary layer conditions are seen on the ice sheet; however, the stability corrections used by RACMO2.3 and BMF13 are different. For the stable boundary layer, RACMO2.3 uses *Businger et al.* [1971], which is also used for unstable boundary layers in both models, whereas BMF13 uses a universal function produced from yearlong in situ Surface Heat Budget of the Arctic Ocean data in the Arctic [i.e., *Grachev et al.*, 2007], which has shown to be more realistic over ice. The parameterization used in BMF13 has shown to not underestimate the magnitude of the flux in stable boundary layers, unlike the parameterization used by RACMO2.3. Thus, this could add to the slightly larger deposition rates seen in the winter months from BMF13 (Figure 13).

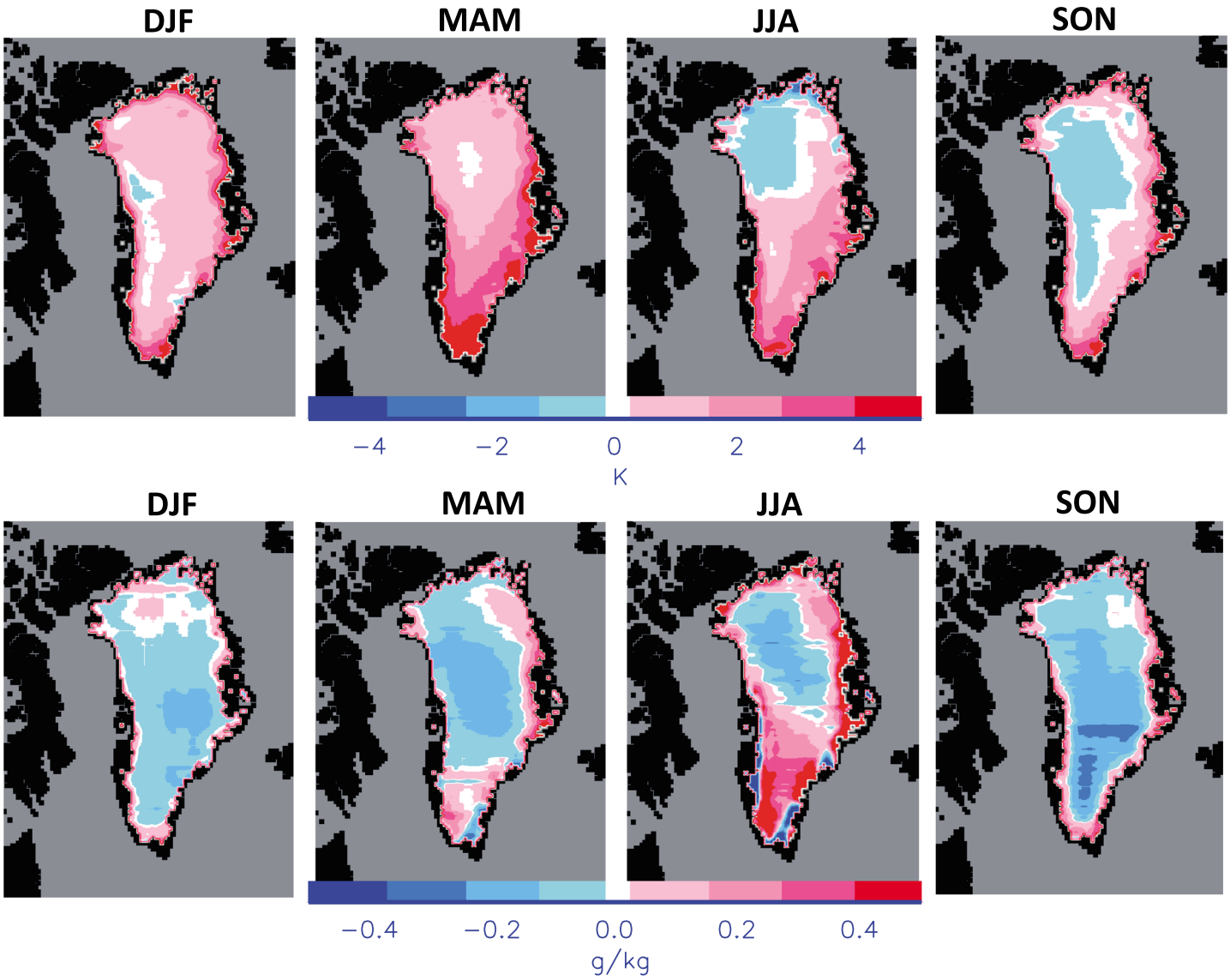

Figure 17. (top row) Average seasonal skin temperature differences between AIRS and RACMO2.3 and (bottom row) average seasonal 2 m specific humidity differences between AIRS and RACMO2.3. Black is land and grey is no data.

RACMO2.3 uses eddy transfer coefficients based on *Louis* [1979], where the coefficients are related to the Richardson number. The BMF13 model uses bulk transfer coefficients from *Launiainen and Vihma* [1990], where coefficients are related to the roughness of the surface, which we get from the MISR roughness length product.

In RACMO2.3, the roughness lengths for momentum (z_0) is set to 1 mm for the snow-covered ice sheet and 5 mm for bare glacial ice, and cannot be larger than 100 mm for the tundra surface type. In BMF13, z_0 is dependent on the snow/ice surface roughness, which we get from the MISR roughness product, discussed

Table 6. Coefficients for Estimating the Scalar Roughness Lengths in the Three Aerodynamic Regimes

Re	B_0	B_1	B_2
$Re < 0.135$ (smooth)	1.43	0	0
$0.135 < Re < 2.5$ (transition)	0.25	−0.589	0
$2.5 < Re < 1000$ (rough)	0.356	−0.538	−0.181

Table 7. Polynomial Coefficients for Calculating z_T

Re	B_0	B_1	B_2
$Re < 0.135$ (smooth)	1.25	0	0
$0.135 < Re < 2.5$ (transition)	0.149	−0.550	0
$2.5 < Re < 1000$ (rough)	0.317	−0.565	−0.183

previously. This product, which only has values in the sunlit months and where the largest values occur along the edge of the ice sheet and at the lowest elevations (Figure 1d), is where we see the largest differences in the vapor flux between the two models (Figure 16).

Both RACMO2.3 and BMF13 compute (3) the roughness lengths of heat and humidity based on *Andreas* [1987], which depend on the roughness Reynolds number.

$$\ln(z_T) = \ln(z_q) = \ln(z_0) + b_0(Re) + b_1(Re)\ln(Re) + b_2(Re)(\ln(Re))^2 \tag{3}$$

Where for RACMO2.3 the flow is classified as smooth, transition, and rough depending on Reynolds number (Table 6). However, *Andreas et al*. [2005] found that different polynomial coefficients for z_T and z_q are needed because the molecular diffusivity of heat in air is less than the molecular diffusivity of water vapor in air. Thus, in BMF13, these are calculated from (3), but the coefficients are different and are shown in Tables 7 and 8.

5.2. Data Differences

Differences in the model forcing data will also cause differences in the magnitudes of the vapor flux. Although both AIRS and RACMO2.3 temperature and humidity products have proved to have small errors when compared to AWS station data, they may have larger differences when comparing them over the entire GrIS. Figure 17 shows the difference between AIRS and RACMO2.3 skin temperatures across the ice sheet. RACMO2.3 skin temperatures are on average 1.25 K lower than AIRS for all elevations (Figure 13). AIRS has higher skin temperatures than RACMO2.3 in the winter months (DJF ~1.3 K) over the majority of the ice sheet and has slightly higher skin temperatures in the fall (~0.6 K), with lower temperatures on the western side of the ice sheet. In the spring and summer, AIRS has much higher skin temperatures than RACMO2.3, with the largest differences occurring in the spring, ~2.1 K compared to ~1.0 K in the summer. In the summer, AIRS has slightly lower skin temperatures in the northwest part of the ice sheet compared to RACMO2.3. Higher skin temperatures from AIRS could cause higher rates of sublimation as long as the specific humidity is low.

These differences are likely caused by how the skin temperature products are produced. For example, RACMO2.3 derives the skin temperature from closure of the surface energy balance equation, which is different for each surface type. Errors could arise due to the accuracy of the terms in the surface energy balance equation, like the amount of incoming shortwave radiation [*Kuipers Munneke et al*., 2011] or the albedo of the surface [*Ettema et al*., 2010b]. The AIRS skin temperature product, where all surfaces are treated the same, is solved for by removing spurious errors in the retrievals [*Susskind et al*., 2014]. Components potentially affecting the temperature from AIRS are blowing snow and the amount of clouds/water vapor in the atmosphere that would affect the retrieval.

In RACMO2.3, the lowest model level is a hybrid sigma level with different height over topography. Once fluxes are calculated, the model outputs the humidity at 2 m using similarity theory described in *Dyer* [1974]. The BMF13 model uses the similarity theory and an iterative calculation scheme of *Launiainen and Vihma* [1990] to determine the air temperature and humidity at 2 m from the AIRS products at the closest pressure level to the surface of the ice sheet. Thus, errors could arise in both derivations of the 2 m data products used to calculate the flux.

Table 8. Polynomial Coefficients for Calculating z_q

Re	B_0	B_1	B_2
$Re < 0.135$ (smooth)	1.61	0	0
$0.135 < Re < 2.5$ (transition)	0.351	−0.628	0
$2.5 < Re < 1000$ (rough)	0.396	−0.512	−0.180

The largest differences of 2 m specific humidity (Figure 17) are found in JJA where the specific humidity from AIRS is 0.13 g kg^{-1} higher than that from RACMO2.3 at all elevations except for those above 3000 m asl (−0.11 g kg^{-1}). The largest differences in specific humidity occur at elevations between 300 m and 1500 m asl (0.28 g kg^{-1}). Like the skin temperature, the specific humidity from AIRS is lower than RACMO2.3 in the northwest region of the ice sheet. The spring is similar to the summer, except that the magnitude of the differences is smaller and the area where the specific humidity from AIRS is drier has increased. In SON and DJF, the 2 m specific humidity from AIRS is lower than RACMO2.3, with the largest differences occurring at high elevations. At the highest elevations (greater than 3000 m asl), RACMO2.3 has higher values for the entire year, while differences are largest in the fall.

In the winter months, even though the skin temperatures and 2 m specific humidities are higher in RACMO2.3 than AIRS, the magnitude of the differences between the specific humidity at the surface and 2 m between the two data products are similar and thus the deposition rates of the two models are similar. In MAM, since the skin temperatures from AIRS are higher than from RACMO2.3, and the 2 m specific humidity is lower at higher elevations, the sublimation rates are higher from BMF13 at elevations greater than 3000 m asl (Figure 14). In the summer months, the specific humidity from AIRS is higher than that from RACMO2.3, especially along the southern regions of the ice sheet. While skin temperatures from AIRS are also higher in this region, their specific humidity difference in magnitude remains smaller than that from RACMO2.3, leading to the differences in sublimation between the two models. This keeps the specific humidity gradient between the surface and 2 m smaller than in RACMO2.3, and sublimation rates are lower in BMF13. In SON, 2 m specific humidity from AIRS is much lower than RACMO2.3, especially at high elevations, which, along with higher skin temperatures, causes the magnitude of the positive vapor flux to drop off more slowly in BMF13 compared to RACMO2.3 (see Figure 14).

Overall, specific humidity from AIRS tends to be lower in all seasons at elevations greater than 3000 m asl, and for all elevations in the winter months. In contrast, AIRS shows higher humidity in the spring and summer months along the southern tip of the ice sheet, corresponding with comparisons of specific humidity at the South Dome GC-Net Station and QAS_U and TAS_U PROMICE stations. Skin temperatures from AIRS are higher in the spring and summer months, but lower in the winter months. Despite these differences between AIRS and RACMO2.3, the magnitudes and behavior of the vapor flux at all elevations are very similar. Differences at the surface tend to be comparable with differences at 2 m, resulting in a similar gradient.

6. Conclusions

The goal of this study was to produce a vapor flux data set for the Greenland ice sheet using remotely sensed data from AIRS, which are used as input for a vapor flux model. This allows for full coverage of the entire ice sheet, compared to point measurements from automatic weather stations, and allows for independent comparison with regional climate models, which use reanalysis data as boundary conditions. The results from this method produced an average 14.6 ± 3.6 Gt yr^{-1} loss due to sublimation over the entire GrIS. While this amount is comparable with results from RACMO2.3 [*Lenaerts et al.*, 2012], they are about an order of magnitude less than those from *Box and Steffen* [2001]. Using in situ observations from GC-Net, *Box and Steffen* [2001] estimated the sublimation via extrapolation from only a few point measurements across the ice sheet, and while these data might be more accurate at these sites, they claimed that they likely overpredict the total sublimation from GrIS (54% uncertainty) in areas where no in situ data exist, especially at low elevations where the sublimation is highest. No single method to estimate the vapor flux on the Greenland ice sheet is expected to be perfect and many uncertainties remain. A downside of the AIRS data is that the footprint is much larger than that of RACMO2.3 and the temporal scale is only twice daily, and because of this AIRS probably misses some variations in the temperature and humidity that RACMO2.3 captures. Regardless of these shortcomings, the blended AIRS 2 m air temperature and specific humidity data and the skin temperature displays small errors compared with the GC-Net and PROMICE in situ observations. A combined uncertainty of 44% in the BMF13 vapor flux product was found, and not including the southeast coastal stations, the RMSE is reduced to 25%.

We find that the vapor flux is a relatively small but nonnegligible component of the Greenland surface mass balance (14.6 ± 3.6 Gt/yr in 2003–2014, equivalent to 6 ± 2% of the SMB between 2003 and 2014). Although no trends in the vapor flux were found over the 2003–2014 period, there were larger interannual variations.

The BMF13 vapor flux peaks in the summer (sublimation), with yearly variations in the flux attributed to different atmospheric conditions seen regionally across the ice sheet. Summers where there were larger areas of surface melt, especially when coinciding with lower humidity, led to higher vapor flux rates, enhancing surface mass loss. The largest fluxes occurred in the southeastern portion of the ice sheet (regions 4–6) in the ablation zones and in elevations between 1500 and 3000 m asl. Fluxes decreased with increasing elevation and increasing latitude. Deposition, having a much smaller magnitude than sublimation/evaporation, occurs during the winter months.

When compared with the BMF13 vapor flux data, RACMO2.3 agreed qualitatively well on both a spatial and temporal scale. The largest differences in magnitude occurred in the summer months at elevations lower than 3000 m asl, where the magnitude of the flux from RACMO2.3 was slightly larger than that from BMF13. Regionally, the largest differences occurred in the southeastern areas of GrIS (regions 4–6). These differences are due to the fact that AIRS overestimates temperature and humidity near the coast, where there is contamination of open-ocean waters and large subgrid heterogeneity in the AIRS footprint, which is much larger than RACMO2.3.

Many uncertainties remain with respect to future changes in the near surface humidity and precipitation amounts/patterns over the Greenland ice sheet when the climate warms, however. This complicates future projections of changes in the vapor flux and their impact on Greenland ice sheet surface mass balance. If precipitation were to decrease in the future, then the vapor flux might play a larger role in the surface mass balance than it does presently. Our results can help reduce the uncertainty of the vapor flux and hence the surface mass balance produced by regional climate models, since our results are independent, encompass the entire ice sheet, and have proven to be robust. This is important for future projections of mass loss from GrIS and its contribution to sea level rise.

Acknowledgments
The work of Linette Boisvert and Jae Lee was funded by NASA ROSES 2012 IDS proposal: 12-IDS12-0120. This study is funded by Utrecht University through its strategic theme, Sustainability, Subtheme Water, Climate and Ecosystems. This work was carried out under the program of the Netherlands Earth System Science Centre (NESSC), financially supported by the Ministry of Education, Culture and Science (OCW). J.T.M.L. is supported by NWO ALW through a Veni postdoctoral grant. B.N. and M.R.v.d.B. acknowledge support from the Polar Program of NOW. Data from AIRS can be found at www.airs.jpl.nasa.gov. RACMO2.3 output is freely available by request to Michiel van den Broeke (m.r.vandenbroeke@uu.nl). The MISR roughness data product can be obtained from Anne Nolin (anne.nolin@gmail.com). The authors would like to thank Konrad Steffen for providing the GC-Net station data, which can be found at cires1.colorado.edu/steffen/gcnet. PROMICE data can be found readily available at: http://www.promice.dk/. The authors would like to thank the anonymous reviewers for providing very helpful comments and feedback on this manuscript.

References

Ahlstrom, A. P., et al. (2008), A new programme for monitoring the mass loss of the Greenland ice sheet, *Geol. Surv. Denmark Greenland Bull.*, *15*, 61–64.

Andersen, S. B., A. P. Ahlstrom, M. L. Andersen, M. Citterio, C. Charalampidis, K. Edelvang, K. Haubner, S. H. Larsen, M. Viechers, and A. Weidick (2015), Greenland ice sheet melt area from MODIS (2000–2014), *Geophys. Surv. Denmark Greenland Bull.*, *33*, 57–60.

Andreas, E. L. (1987), Spectral measurements in a disturbed boundary layer over snow, *J. Atmos. Sci.*, *44*, 1912–1939, doi:10.1175/1520-0469(1987)044<1912:SMIADB>2.0.CO;2.

Andreas, E. L., R. E. Jordan, and A. P. Makhtas (2005), Parameterizing turbulent exchange over sea ice: The ice station Weddell results, *Boundary Layer Meteorol.*, *114*, 439–460.

Andreas, E. L., P. O. G. Persson, R. E. Jordan, T. W. Horst, P. S. Guest, A. A. Grachev, and C. W. Fairall (2010), Parameterizing turbulent exchange over sea ice in winter, *J. Hydrometeorol.*, *11*, 87–104.

Bennartz, R., M. D. Shupe, D. D. Turnery, V. P. Walden, K. Steffen, C. J. Cox, M. S. Kulie, N. B. Miller, and C. Pettersen (2013), July 2012 Greenland melt extent enhanced by low-level liquid clouds, *Nature*, *496*, 83–86, doi:10.1038/nature12002.

Blackwell, W. J. (2012), Neural network Jacobian analysis for high-resolution profiling of the atmosphere, *EURASIP J. Adv. Signal Process.*, *2012*, 71, doi:10.1186/1687-6180-2012-71.

Boisvert, L. N., T. Markus, and T. Vihma (2013), Moisture flux changes and trends for the entire Arctic in 2003–2011 derived from EOS Aqua data, *J. Geophys. Res. Oceans*, *118*, 5829–5843, doi:10.1002/jgrc.20414.

Boisvert, L. N., D. L. Wu, T. Vihma, and J. Susskind (2015a), Verification of air/surface humidity differences from AIRS and ERA-Interim in support of turbulent flux estimation in the Arctic, *J. Geophys. Res. Atmos.*, *120*, 2169–8996, doi:10.1002/2014JD021666.

Boisvert, L. N., D. L. Wu, and C.-L. Shie (2015b), Increasing evaporation amounts seen in the Arctic between 2003–2013 from AIRS data, *J. Geophys. Res. Atmos.*, *120*, 6865–6881, doi:10.1002/2015JD023258.

Box, J. E., and K. Steffen (2001), Sublimation on the Greenland ice sheet from automated weather station observations, *J. Geophys. Res.*, *106*, 33,965–33,981, doi:10.1029/2001JD900219.

Businger, J. A., J. C. Wyngaard, Y. Izumi, and E. F. Bradley (1971), Flux-profile relationships, *J. Atmos. Sci.*, *28*, 181–189.

Chen, J. L., C. R. Wilson, and B. D. Tapley (2006), Satellite Gravity measurements confirm accelerated melting of Greenland ice sheet, *Science*, *313*(5795), 1958–1960, doi:10.1126/science.1129007.

Cronin, M. F., C. W. Fairall, and M. J. McPhaden (2006), An assessment of buoy derived and numerical weather prediction of surface heat fluxes in the tropical Pacific, *J. Geophys. Res.*, *111*, C06038, doi:10.1029/2005JC003324.

Dee, D. P., et al. (2011), The ERA-Interim reanalysis: Configuration and performance of the data assimilation system, *Q. J. R. Meteorol. Soc.*, *137*, 553–597, doi:10.1002/qj.828.

DiMarzio, J., A. Brenner, R. Schutz, C. A. Shuman, and H. J. Zwally (2007), *GLAS/ICESat 1 km Laser Altimetry Digital Elevation Model of Greenland*, Natl. Snow and Ice Data Cent., Digital media, Boulder, Colo.

Dong, S., S. T. Gille, J. Sprintall, and E. J. Fetzer (2010), Assessing the potential of the Atmospheric Infrared Sounder (AIRS) surface temperature and specific humidity in turbulent heat flux estimates in the Southern Ocean, *J. Geophys. Res.*, *115*, C05013, doi:10.1029/2009JC005542.

Dyer, A. J. (1974), A review of flux-profile relationships, *Boundary Layer Meteorol.*, *7*, 363–372.

Echelmeyer, K., T. Clarke, and W. Harrison (1991), Surficial glaciology of Jakobshavns Isbrae, West Greenland: Part I. Surface morphology, *J. Glaciol.*, *37*(127), 368–382.

ECMWF-IFS (2008), Part IV: Physical processes (CY33R1), Technical Report.

Enderlin, E. M., I. M. Howat, S. Jeong, M.-J. Noh, J. H. van Angelen, and M. R. van den Broeke (2014), An improved mass budget for the Greenland ice sheet, *Geophys. Res. Lett.*, *41*, 866–872, doi:10.1002/2013GL059010.

Ettema, J., M. R. van den Broeke, E. van Meijgaard, W. J. van de Berg, J. E. Box, and K. Steffen (2010a), Climate of the Greenland ice sheet using a high-resolution climate model—Part 1: Evaluation, *Cryosphere*, *4*, 511–527, doi:10.5194/tc-4-511-2010.

Ettema, J., M. R. van den Broeke, E. van Meijgaard, and W. J. van de Berg (2010b), Climate of the Greenland ice sheet using a high-resolution climate model—Part 2: Near-surface climate and energy balance, *Cryosphere*, *4*, 529–544, doi:10.5194/tc-4-529-2010.

Fettweis, X., E. Hanna, C. Lang, A. Belleflamme, M. Erpicum, and H. Gallee (2013), Important role of the mid-tropospheric atmospheric circulation in the recent surface melt increase over the Greenland ice sheet, *Cryosphere*, *7*, 241–248, doi:10.5194/tc-7-241-2013.

Grachev, A. A., E. L. Andreas, C. W. Fairall, P. S. Guest, and P. O. G. Persson (2007), SHEBA flux-profile relationships in the stable atmospheric boundary layer, *Boundary Layer Meteorol.*, *124*, 315–333, doi:10.1007/s10546-007-9177-6.

Hall, D. K., J. C. Comiso, N. E. DiGirolamo, C. A. Shuman, J. E. Box, and L. S. Koenig (2013), Variability in the surface temperature and melt extent of the Greenland ice sheet from MODIS, *Geophys. Res. Lett.*, *40*, 2114–2120, doi:10.1002/grl.50240.

Hanna, E., P. Huybrechts, K. Steffen, J. Cappelen, R. Huff, C. Shuman, T. Irvine-Fynn, S. Wise, and M. Griffiths (2008), Increased runoff from melt from the Greenland ice sheet: A response to global warming, *J. Clim.*, *21*, 331–341, doi:10.1175/2007JCLI1964.1.

He, T., S. Liang, Y. Yu, D. Wang, F. Gao, and Q. Liu (2013), Greenland surface albedo changes in July 1981–2012 from satellite observations, *Environ. Res. Lett.*, *8*(4), doi:10.1088/1748-9326/8/4/044043.

Howat, I. M., I. Joughin, and T. A. Scambos (2007), Rapid changes in ice discharge from Greenland outlet glaciers, *Science*, *315*(5818), 1559–1561, doi:10.1126/science.1138478.

Jakobson, E., T. Vihma, T. Palo, L. Jakobson, H. Keernik, and J. Jaagus (2012), Validation of atmospheric reanalyses over the central Arctic Ocean, *Geophys. Res. Lett.*, *39*, L10802, doi:10.1029/2012GL051591.

Johannessen, O. M., K. Khvorostovsky, M. W. Miles, and L. P. Bobylev (2005), Recent ice-sheet growth in the interior of Greenland, *Science*, *310*(5750), 1013–1016, doi:10.1126/science.1115356.

Kahn, S. A., et al. (2014), Sustained mass loss of the northeast Greenland ice sheet triggered by regional warming, *Nat. Clim. Change*, *4*, 292–299, doi:10.1038/nclimate2161.

Kuipers Munneke, P., M. R. van den Broeke, J. T. M. Lenaerts, M. G. Flanner, A. S. Gardner, and W. J. van de Berg (2011), A new albedo parameterization for use in climate models over the Antarctic ice sheet, *J. Geophys. Res.*, *116*, D05114, doi:10.1029/2010JD015113.

Launiainen, J., and T. Vihma (1990), Derivation of the turbulent surface fluxes—An iterative flux-profile method allowing arbitrary observing heights, *Environ. Software*, *5*, 113–124.

Lenaerts, J. T. M., M. R. van den Broeke, J. H. van Angelen, E. van Meijgaard, and S. J. Dery (2012), Drifting snow climate of the Greenland ice sheet: A study with a regional climate model, *Cryosphere*, *6*, 891–899, doi:10.5194/tc-6-891-2012.

Louis, J.-F. (1979), A parametric model of vertical eddy fluxes in the atmosphere, *Boundary Layer Meteorol.*, *17*(2), 187–202.

Mernild, S. H., T. L. Mote, and G. E. Liston (2011), Greenland ice sheet surface melt extent and trends: 1960–2010, *J. Glaciol.*, *57*(204), 621–628, doi:10.3189/002214311797409712.

Mernild, S. H., E. Hanna, J. R. McConnell, M. Sigl, A. P. Beckerman, J. C. Yde, J. Cappelen, J. K. Malmros, and K. Steffen (2015), Greenland precipitation trends in a long-term instrumental climate context (1890–2012): Evaluation of coastal and ice core records, *Int. J. Climatol.*, *35*, 303–320, doi:10.1002/joc.3986.

Mote, T. L. (2007), Greenland surface melt trends 1973–2007: Evidence of a large increase in 2007, *Geophys. Res. Lett.*, *34*, L22507, doi:10.1029/2007GL0.1976.

Neff, W., G. P. Compo, F. M. Ralph, and M. D. Shupe (2014), Continental heat anomalies and the extreme melting of the Greenland ice surface in 2012 and 1889, *Geophys. Res. Lett.*, *119*, 6520–6536, doi:10.1002/2014JD021470.

Nghiem, S. V., D. K. Hall, T. L. Mote, M. Tedesco, M. R. Albert, K. Keegan, C. A. Shuman, N. E. DiGirolamo, and G. Neumann (2012), The extreme melt across the Greenland ice sheet in 2012, *Geophys. Res. Lett.*, *39*, L20502, doi:10.1029/2012GL053611.

Noel, B., W. J. van de Berg, E. van Meijgaard, P. Kuipers Menneke, R. S. W. van de Wal, and M. R. van den Broeke (2015), Evaluation of the updated regional climate model RACMO2.3: Summer snowfall impact on the Greenland ice sheet, *Cryosphere*, *9*, 1831–1844, doi:10.5194/tc-9-1831-2015.

Nolin, A. W., F. M. Fetterer, and T. A. Scambos (2002), Surface roughness characterizations of sea ice and ice sheets: Case studies with MISR data, *IEEE Trans. Geosci. Remote Sens.*, *40*(7), 1605–1615, doi:10.1109/TGRS,2002.801581.

Ohmura, A., P. Calanca, M. Wild, and M. Anklin (1999), Precipitation, accumulation, and mass balance of the Greenland ice sheet, *Z. Gletsch. Glazialgeol.*, *35*(1), 1–120.

Salesky, S. T., and M. Chamecki (2012), Random errors in turbulence measurements in the atmospheric surface layer: Implications for the Monin-Obhukov similarity theory, *J. Atmos. Sci.*, *69*(12), 3700–3714, doi:10.1175/JAS-D-12-096.1.

Schuenemann, K. C., and J. J. Cassano (2010), Changes in synoptic weather patterns and Greenland precipitation in the 20th and 21st centuries: 2. Analysis of 21st century atmospheric changes using self-organizing maps, *J. Geophys. Res.*, *115*, D05108, doi:10.1029/2009JD011706.

Seo, K.-W., D. E. Waliser, C.-K. Lee, B. Tian, T. Scambos, B.-M. Kim, J. H. van Angelen, and M. R. van den Broeke (2015), Accelerated mass loss from Greenland ice sheet: Links to atmospheric circulation in the North Atlantic, *Global Planet. Change*, *128*, 61–71, doi:10.1016/j.gloplacha.2015.02.006.

Shepherd, A., et al. (2012), A reconciled estimate of ice-sheet mass balance, *Science*, *338*(6111), 1183–1189, doi:10.1126/science.1228102.

Smeets, C. J. P. P., and M. R. van den Broeke (2008), Temporal and spatial variations of the aerodynamic roughness length in the ablation zone of the Greenland ice sheet, *Boundary Layer Meteorol.*, *128*, 315–338, doi:10.1007/s10546-008-9291-0.

Sneed, W. A., and G. S. Hamilton (2007), Evolution of melt pond volume on the surface of the Greenland ice sheet, *Geophys. Res. Lett.*, *34*, L03501, doi:10.1029/2006GL028697.

Steffen, K., J. E. Box, and W. Abdalati (1996), Greenland Climate Network: GC-Net, in *CRREL 96–27 Special Report on Glaciers, Ice Sheets and Volcanoes (tribute to M. Meier)*, edited by S. C. Colbeck, pp. 98–103, US Army, Hanover, N. H.

Sundal, A. V., A. Shepherd, P. Nienow, E. Hanna, S. Palmer, and P. Huybrechts (2011), Melt-induced speed-up of Greenland ice sheet offset by efficient subglacial drainage, *Nature*, *469*, 521–524, doi:10.1038/nature09740.

Susskind, J., C. D. Barnet, and J. M. Blaisdell (2003), Retrieval of atmospheric and surface parameters from AIRS/AMSU/HSB data in the presence of clouds, *IEEE Trans. Geosci. Remote Sens.*, *41*(2), 390–409, doi:10.1109/TGRS.2002.808236.

Susskind, J., J. M. Blaisdell, L. Iredell, and F. Keita (2011), Improved temperature sounding and quality control methodology using AIRS/AMSU data: The AIRS science team version 5 retrieval algorithm, *IEEE Trans. Geosci. Remote Sens.*, *49*(3), 883–907, doi:10.1109/TGRS.2010.2070508.

Susskind, J., J. M. Blaisdell, and L. Iredell (2014), Improved methodology for surface and atmospheric soundings, error estimates, and quality control procedures: The atmospheric infrared sounder science team version-6 retrieval algorithm, *J. Appl. Remote Sens.*, *8*(1), 084994, doi:10.1117/1.JRS.8.084994.

Tedesco, M., X. Fettweis, M. R. van den Broeke, R. S. W. van de Wal, C. J. P. P. Smeets, W. J. van de Berg, M. C. Serreze, and J. E. Box (2011), The role of albedo and accumulation in the 2010 melting record in Greenland, *Environ. Res. Lett.*, *6*, 014005, doi:10.1088/1748-9326/6/1/014005.

Unden, P., et al. (2002), HIRLAM-5 scientific documentation, HIRLAM-5 Project Report, SMHI, 146 p.

Van Angelen, J. H., J. T. M. Lenaerts, S. Lhermitte, X. Fettweis, P. Kuipers Munneke, M. R. van den Broeke, E. van Meijgaard, and C. J. P. P. Smeets (2012), Sensitivity of Greenland ice sheet surface mass balance to surface albedo parameterization: A study with a regional climate model, *Cryosphere*, *6*, 1175–1186, doi:10.5194/tc-6-1175-2012.

Van den Broeke, M., J. Bamber, J. Ettema, E. Rignot, E. Schrama, W. J. van de Berg, E. van Meijgaard, I. Velicogna, and B. Wouters (2009), Partitioning recent Greenland mass loss, *Science*, *326*(5955), 984–986, doi:10.1126/science.1178176.

Van Wessem, J. M., C. H. Reijmer, J. T. M. Lenaerts, W. J. van de Berg, M. R. van den Broeke, and E. van Meijgaard (2014), Updated cloud physics in a regional atmospheric climate model improves the modeled surface energy balance of Antarctica, *Cryosphere*, *8*, 125–135, doi:10.5194/tc-8-125-2014.

Velicogna, I., T. C. Sutterly, and M. R. van den Broeke (2014), Regional acceleration in ice mass loss from Greenland and Antarctica using GRACE time-variable gravity data, *J. Geophys. Res. Space Physics*, *119*, 8130–8137, doi:10.1002/2014GL061052.

Vizcaino, M., W. H. Lipscomb, W. J. Sacks, and M. van den Broeke (2014), Greenland Surface mass balance at simulated by the community earth system model. Part II: Twenty-first-century changes, *J. Clim.*, *27*, 215–226, doi:10.1175/JCLI-D-12-00588.1.

Wang, W., J. Li, and H. J. Zwally (2014), Dynamic inland propagation of thinning due to ice loss at the margins of the Greenland ice sheet, *J. Glaciol.*, *58*(210), doi:10.3189/2012JoG11J187.

Woldemeskel, F. M., A. Sharma, B. Sivakumar, and R. Mehrotra (2012), An error estimation method for precipitation and temperature projects for future climates, *J. Geophys. Res.*, *117*, D22103, doi:10.1029/2012JD018062.

Wouters, B., D. Chambers, and E. J. O. Schrama (2008), GRACE observes small-scale mass loss in Greenland, *Geophys. Res. Lett.*, *35*, L20501, doi:10.1029/2008GL034816.

Zwally, H. J., et al. (2011), Greenland ice sheet mass balance: Distribution of increased mass loss with climate warming; 2003–07 versus 1992–2002, *J. Glaciol.*, *57*(201), 88–102, doi:10.3189/002214311795306682.